



# A front tracking method for direct numerical simulation of evaporation process in a multiphase system

Muhammad Irfan, Metin Muradoglu \*

Department of Mechanical Engineering, Koc University, Rumelifeneri Yolu, Sariyer 34450 Istanbul, Turkey

## ARTICLE INFO

### Article history:

Received 19 August 2016

Received in revised form 27 December 2016

Accepted 13 February 2017

Available online 20 February 2017

### Keywords:

Evaporation

Phase change

Front-tracking method

Multi-phase flows

The Clausius–Clapeyron relation

One-field formulation

## ABSTRACT

A front-tracking method is developed for the direct numerical simulation of evaporation process in a liquid–gas multiphase system. One-field formulation is used to solve the flow, energy and species equations in the framework of the front tracking method, with suitable jump conditions at the interface. Both phases are assumed to be incompressible; however, the divergence-free velocity field condition is modified to account for the phase-change/mass-transfer at the interface. Both temperature and species gradient driven evaporation/phase-change processes are simulated. For the species gradient driven phase change process, the Clausius–Clapeyron equilibrium relation is used to find the vapor mass fraction and subsequently the evaporation mass flux at the interface. A number of benchmark cases are first studied to validate the implementation. The numerical results are found to be in excellent agreement with the analytical solutions for all the studied cases. The methods are then applied to study the evaporation of a static as well as a single and two droplets systems falling in the gravitational field. The methods are demonstrated to be grid convergent and the mass is globally conserved during the phase change process for both the static and moving droplet cases.

© 2017 Elsevier Inc. All rights reserved.

## 1. Introduction

Interfacial flows are frequent occurrences in nature, industrial processes and biological systems. Air/gas bubbles rising in a water bed under buoyancy, a free-falling rain droplet in air, core annular flows for oil/gas transportation in petroleum industries, breathing system in living organisms are some of the examples involving multiphase flows; where interfaces move, deform and even topological changes occur during the course of time. In addition to experiments, the numerical simulations have become an indispensable tool for the medical and the industrial sector to help improve their products and system designs for maximum efficiency. Over decades, researchers have developed various numerical techniques to simulate multiphase flows. It is quite a challenging task to simulate multiphase flows in the sense that sharp property gradients exist across the interfaces, which evolve and undergo substantial deformations including topological changes.

Harlow and Welch [1] proposed one of the first methods to simulate free surface flows: the marker and cell method. Hirt and Nichols [2] came up with a memory efficient region-following scheme, called the volume of fluid (VOF) method, with single value of fluid volume fraction in each mesh cell. Interface can also be viewed as a level set function; the technique has been successfully implemented by various authors to simulate multiphase flows [3,4]. In order to keep the level set function continuous and well resolved, the level set function is maintained as a signed distance function for all the

\* Corresponding author.

E-mail address: mmuradoglu@ku.edu.tr (M. Muradoglu).

time, without reconstructing the interface [4]. The notion of diffuse interface has also been used to model the interfacial flows [5]. Jacqmin [6] performed critical test cases to show the ability of the phase field method to simulate two phase flows. All the above mentioned methods fall under the category of interface capturing method. The second category may be called as interface tracking method, in which the interface is represented by a separate Lagrangian grid, whereas the governing equations are solved on the background Eulerian mesh. In some earlier implementations, the moving interface is tracked by modifying the background Eulerian grid near the interface such that the fixed grid lines follow the interface [7,8]. Tryggvason et al. [9,10] devised a front tracking method, which does not require any re-meshing of the background grid to track the interface. Rather, the interface or front is explicitly tracked by interpolating the velocity field from the Eulerian grid onto the interface marker points.

The phase change phenomenon adds another dimension to the interfacial flows and thus makes modeling even more challenging. Condensation, solidification, dissolution, boiling and vaporization/evaporation are different phase change processes that are frequently encountered in nature and industrial applications. Design of heat exchangers and boilers for efficient heat transfer, achieving uniform material properties through casting process, efficient burning of fuel droplets in internal combustion engines and the dissolution of drugs in human body are some of the application areas, where a better understanding of the physical processes and the design parameters is expected to result in increased system efficiencies and better health standards. Direct numerical simulation is a promising technique to simulate and analyze the designs for the system performance under a wide range of operating parameters. Also, with the advent of micro and nano-scale applications, the direct numerical simulation has proven to be an efficient tool in design improvement of the systems, where experimentation has serious limitations [11].

Researchers have applied different multiphase flow modeling techniques to simulate different phase change phenomena. Welch and Wilson [12] studied horizontal film boiling problem using a VOF method. Detailed numerical simulation of 3D evaporating and strongly deformed droplet was performed by Schlottke and Weigand [13] using the VOF method. Film boiling case has been studied using a level set method by Son and Dhir [14] and Gibou et al. [15]. The level set method, in combination with the ghost fluid method [16], has been used to simulate evaporation of a moving and deforming droplet by Tanguy et al. [17]. Another promising tool to model and simulate multiphase flow is the lattice Boltzmann method. Safari et al. incorporated the temperature [18] and species gradient [19] based phase change models into the lattice Boltzmann method developed by Lee [20].

The original front-tracking method developed for isothermal multifluid flows by Tryggvason and coworkers [9,10] has been extended by various researchers to include the mass transfer and the phase change phenomena. For example, Juric and Tryggvason [21] simulated the film boiling. They used an iterative procedure to set the correct temperature boundary condition at the interface. The same procedure has also been used to track the flame front of a premixed flame by Qian et al. [22]. Esmaeeli and Tryggvason [23,24] eliminated the iterative algorithm by setting the interface temperature as the saturation temperature at the system pressure. Koynov et al. [25] performed simulations of a single bubble and bubble swarms rising due to buoyancy including mass transfer and chemical reactions at different operating conditions. Aboulhasanzadeh et al. [26] have recently developed a multiscale approach to compute the mass transfer from buoyant bubbles using a boundary-layer approximation next to the bubble. This approach greatly reduced the overall grid resolution requirement. The front tracking method with phase change model has mostly been applied to film boiling [21,24] and dendritic solidification [27–29]; the phase change being driven solely by the temperature gradient. But little has been done for moving and deforming liquid droplet vaporization/evaporation. In particular, to the best of our knowledge, the species gradient driven phase-change process has not been modeled in the front-tracking framework.

In this paper, a front tracking method is developed for the liquid droplet evaporation driven by the temperature or species gradient. A one-field formulation is used to solve the governing equations in the framework of the finite-difference/front-tracking method on a fixed, uniform Cartesian grid. Temperature gradient driven phase change model is discussed first. The implementation is validated using two benchmark cases: The Stefan and the sucking interface problems. The numerical results of the interface location, temperature profile and the velocity field show excellent agreement with the analytical results. The cases of 2D static and moving droplet evaporation are then simulated and results are presented. The main novelty of the present work is the species gradient based phase change model. This model can handle a more general situation where the gradient in the species concentration drives phase change, even if the temperature is the same in both the phases, e.g., water droplet evaporating in the air at the atmospheric conditions. The Clausius–Clapeyron relation is incorporated to compute the species mass fraction as well as the evaporation mass flux at the interface. Two strategies are compared for implementing the species mass fraction boundary condition at the interface. The one that adds the evaporation mass flux as a source term to the species equation following the strategy used in treating soluble surfactant by Muradoglu and Tryggvason [30,31] is easy to implement, is numerically efficient and yields better results as compared to the one that imposes the species mass fraction at the interface directly as the boundary condition. First, a simplified test case is simulated for which analytical solution is available for the evaporation mass flux. Numerical results agree very well with the analytical solution for various values of interface temperature boundary condition. For a 2D static evaporating droplet case, the model predicts the correct values of equilibrium wet bulb temperature for a water droplet evaporating in the air under various conditions of dry bulb temperature and relative humidity. These results ensure the correct coupling of the Clausius–Clapeyron relation with the solution of the flow, energy and species conservation equations. The model is then applied to simulate the evaporation of droplets that move and undergo significant deformation in a gravitational field. The method has been demonstrated to be grid convergent and the global mass conservation is satisfied for all the above studied cases.

In the next section, the mathematical formulation of the multiphase flow with phase change is presented. The numerical method is described in Section 3 for both evaporation models. In Section 4, a detailed discussion is made about the results of validation cases and other test runs for temperature and species gradient based evaporation. Finally, conclusions are drawn in Section 5.

## 2. Mathematical formulation

Consider a liquid–gas multiphase system; both of which are assumed to be incompressible. Fluid flow in each phase is governed by the Navier–Stokes equations. We can write a single set of governing equations applicable to the whole domain as long as the jumps in the property fields are properly handled across the interface and surface tension effects are taken into account appropriately. Then the momentum conservation equations can be written for the entire computational domain as

$$\frac{\partial \rho \mathbf{u}}{\partial t} + \nabla \cdot (\rho \mathbf{u} \mathbf{u}) = -\nabla p + \rho \mathbf{g} + \nabla \cdot \mu (\nabla \mathbf{u} + \nabla \mathbf{u}^T) + \int_A \sigma \kappa \mathbf{n} \delta(\mathbf{x} - \mathbf{x}_\Gamma) dA, \quad (1)$$

where  $\mathbf{u}$  and  $\mathbf{g}$  are the velocity and the gravitational acceleration vectors, respectively,  $p$  is the pressure,  $t$  is time and  $\rho$  and  $\mu$  are the discontinuous density and viscosity fields, respectively. The last term on the right hand side represents the body force due to the surface tension, where  $\sigma$  is the surface tension coefficient,  $\kappa$  is twice the mean curvature, and  $\mathbf{n}$  is a unit vector normal to the interface. The surface tension acts only on the interface as indicated by the three-dimensional delta function  $\delta$  whose arguments  $\mathbf{x}$  and  $\mathbf{x}_\Gamma$  are the point at which the equation is being evaluated and a point at the interface, respectively.

For a multiphase flow without phase change, the continuity equation satisfies the incompressibility condition throughout the domain, i.e.,  $\nabla \cdot \mathbf{u} = 0$ . However, for the phase change problem, the divergence-free velocity field condition is modified at the interface to account for the phase-change/mass-transfer, so the continuity equation becomes

$$\nabla \cdot \mathbf{u} = \frac{1}{h_{lg}} \left( \frac{1}{\rho_g} - \frac{1}{\rho_l} \right) \int_A \delta(\mathbf{x} - \mathbf{x}_\Gamma) \dot{q}_\Gamma dA_\Gamma. \quad (2)$$

The delta function makes the above equation non-zero at the interface and zero elsewhere. In Eq. (2),  $h_{lg}$  is the latent heat of vaporization and  $\dot{q}_\Gamma$  represents the heat flux per unit time at the interface. Subscripts  $\Gamma$ ,  $l$  and  $g$  represent the interface, the liquid and gas phases of a multiphase system, respectively. The mass and momentum jump conditions at the interface are:

$$\rho_l (\mathbf{u}_l - \mathbf{u}_\Gamma) \cdot \mathbf{n} = \rho_g (\mathbf{u}_g - \mathbf{u}_\Gamma) \cdot \mathbf{n} = \dot{m}_\Gamma, \quad (3)$$

$$\dot{m}_\Gamma (\mathbf{u}_g - \mathbf{u}_l) = (\boldsymbol{\tau}_g - \boldsymbol{\tau}_l) \cdot \mathbf{n} - (p_g - p_l) \mathbf{I} \cdot \mathbf{n} + \sigma \kappa \mathbf{n}, \quad (4)$$

where  $\dot{m}_\Gamma$  is the mass flux per unit time across the interface,  $\boldsymbol{\tau}$  is the stress tensor and  $\mathbf{I}$  is the identity tensor. Note that the Marangoni effects are not considered in this study but can easily be incorporated into the present numerical method [32]. The energy equation is solved in the whole domain and is given by

$$\frac{\partial T}{\partial t} + \mathbf{u} \cdot \nabla T = \frac{\nabla \cdot k \nabla T}{\rho c_p} - \frac{1}{\rho c_p} \left[ 1 - (c_{p,g} - c_{p,l}) \frac{T_{sat}}{h_{lg}} \right] \int_A \delta(\mathbf{x} - \mathbf{x}_\Gamma) \dot{q}_\Gamma dA_\Gamma, \quad (5)$$

where  $T$  is the temperature,  $c_p$  is the specific heat at constant pressure and  $k$  is the thermal conductivity. Subscript  $sat$  denotes the saturation value of the variable. The last term in the above equation incorporates the thermal effects of phase change into the energy equation where the coefficient  $(1 - (c_{p,g} - c_{p,l}) T_{sat}/h_{lg})$  is a constant which modifies the latent heat  $h_{lg}$  due to unequal specific heats of the liquid and gas phases. The convection–diffusion equation for the species evolution in space and time reads as:

$$\frac{\partial Y_\alpha}{\partial t} + \mathbf{u} \cdot \nabla Y_\alpha = \nabla \cdot D_\alpha \nabla Y_\alpha \quad \alpha = 1, 2, \dots, n_s, \quad (6)$$

where  $Y_\alpha$  and  $D_\alpha$  represent the mass fraction and mass diffusion coefficient of species component  $\alpha$ , respectively. In the present study, we consider only one species, the vapor, but the method can be extended to include many species straightforwardly. We solve the species equation only for the vapor phase in the gas domain, outside the liquid droplet.

The energy and species jump conditions must be satisfied to ensure the energy and mass conservation across the interface. These are:

$$\dot{m}_\Gamma h_{lg} = \dot{q}_\Gamma = k_g \left. \frac{\partial T}{\partial n} \right|_g - k_l \left. \frac{\partial T}{\partial n} \right|_l, \quad (7)$$

$$\dot{m}_\Gamma Y_l^\Gamma - \dot{m}_\Gamma Y_g^\Gamma + \rho_g D_\alpha \left. \frac{\partial Y}{\partial n} \right|_\Gamma = 0. \quad (8)$$

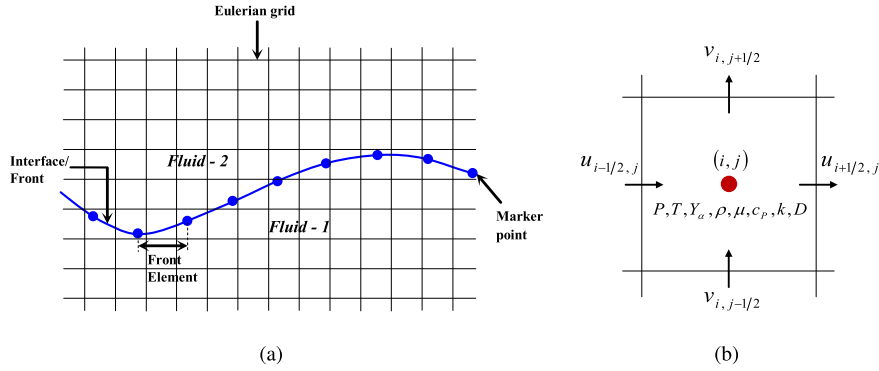


**Fig. 1.** (a) The schematic illustration of a Lagrangian grid on an Eulerian background mesh. (b) The staggered grid used in the numerical solution of the governing equations.

For a mono-component liquid droplet,  $Y_l^\Gamma = 1$  and gradients of the species mass fraction are zero. Thus Eq. (8) takes the form:

$$\dot{m}_\Gamma = \frac{\rho_g D_\alpha \left. \frac{\partial Y_{vap}}{\partial n} \right|_\Gamma^g}{1 - Y_{vap}^\Gamma}. \quad (9)$$

The vapor mass fraction at the interface,  $Y_{vap}^\Gamma$ , is calculated using the Clausius–Clapeyron relation, i.e.,

$$p_{vap}^\Gamma = p_{atm} \exp \left\{ -\frac{h_{lg} m_{vap}}{R} \left( \frac{1}{T^\Gamma} - \frac{1}{T^B} \right) \right\}, \quad (10)$$

$$Y_{vap}^\Gamma = \frac{p_{vap}^\Gamma m_{vap}}{(p_{atm} - p_{vap}^\Gamma) m_g + p_{vap}^\Gamma m_{vap}}, \quad (11)$$

where  $p_{vap}^\Gamma$  is the saturated vapor pressure corresponding to the interface temperature  $T^\Gamma$ ,  $T^B$  is the liquid boiling temperature at the ambient pressure conditions, i.e., at  $p = p_{atm}$ ,  $R$  is the perfect gas constant, and  $m_{vap}$  and  $m_g$  are the molar masses of the vapor and gas, respectively.

We also assume that the material properties remain constant following a fluid particle, i.e.,

$$\frac{D\rho}{Dt} = 0; \quad \frac{D\mu}{Dt} = 0; \quad \frac{Dk}{Dt} = 0; \quad \frac{Dc_p}{Dt} = 0; \quad \frac{DD_\alpha}{Dt} = 0, \quad (12)$$

where  $\frac{D}{Dt} = \frac{\partial}{\partial t} + \mathbf{u} \cdot \nabla$  is the material derivative. The relevant non-dimensional parameters for this study can be expressed as

$$\gamma = \frac{\rho_l}{\rho_g}; \quad \zeta = \frac{\mu_l}{\mu_g}; \quad Sc = \frac{\mu_g}{\rho_g D}; \quad Pr = \frac{\mu c_p}{k};$$

$$Re = \frac{\rho_g u_s l_s}{\mu_g}; \quad St = \frac{c_{p,g} (T_\infty - T_{sat})}{h_{lg}}, \quad (13)$$

where  $\gamma$  and  $\zeta$  represent the density and the viscosity ratios, respectively.  $Sc$ ,  $Pr$ ,  $Re$  and  $St$  are the Schmidt number, Prandtl number, Reynolds number and Stefan number, respectively.  $u_s$  and  $l_s$  are appropriately selected velocity and length scales, respectively, and  $t_s = l_s/u_s$  be the time scale.

### 3. Numerical solution procedure

The governing equations for the flow (Eqs. (1)–(2)), energy (Eq. (5)) and species mass fraction (Eq. (6)) fields are solved in a coupled form on a fixed, uniform, staggered MAC grid using a finite-difference/front-tracking method [9,10,21,24,33]. The spatial derivatives in the momentum equations are discretized using a second-order central difference scheme, whereas, the time integration is performed using a first-order projection method [34]. The solution of the energy and the species equations is advanced in time using a first order explicit Euler method. All spatial derivatives in the energy and species equations are approximated using second-order central differences except for the convective terms where a 5th order WENO-Z [35] scheme is used. The pressure, temperature, species mass fractions and all material properties are stored at the cell centers on an Eulerian grid (Fig. 1(b)).

The interface or front, separating different phases, is made up of connected marker points and is tracked explicitly [9,10,33]. Each marker point moves with the local flow velocity, in addition to the velocity due to phase change, Eqs. (16)–(17).

The piece of the interface between two adjacent marker points is called a front element. The schematic representation of the Lagrangian grid on the background fixed mesh is shown in Fig. 1(a). The Indicator function  $I(\mathbf{x}, t)$  tracks the liquid and the gas phases both in space and time and is defined as:

$$I(\mathbf{x}, t) = \begin{cases} 1 & \text{in droplet phase,} \\ 0 & \text{in bulk phase.} \end{cases} \quad (14)$$

The indicator function  $I(\mathbf{x}, t)$  is computed at each time step using the standard procedure described by Tryggvason et al. [10], which involves the solution of a separable Poisson equation. Then the material property fields are updated at each time step as a function of  $I(\mathbf{x}, t)$

$$\begin{aligned} \rho &= \rho_l I(\mathbf{x}, t) + \rho_g (1 - I(\mathbf{x}, t)); & \mu &= \mu_l I(\mathbf{x}, t) + \mu_g (1 - I(\mathbf{x}, t)); \\ k &= k_l I(\mathbf{x}, t) + k_g (1 - I(\mathbf{x}, t)); & \rho c_p &= \rho_l c_{p,l} I(\mathbf{x}, t) + \rho_g c_{p,g} (1 - I(\mathbf{x}, t)); \\ D_\alpha &= D_{\alpha,g} (1 - I(\mathbf{x}, t)). \end{aligned} \quad (15)$$

Information needs to be communicated between the fixed grid and the moving interface during the solution process. For example, the surface tension as well as the heat and mass fluxes are first calculated at the interface and then smoothed onto the fixed Eulerian grid while solving momentum, energy and species equations, respectively. Similarly, the velocity field is only available at the fixed Eulerian grid nodes and needs to be interpolated onto the marker points for moving the interface. A complete description of the smoothing and interpolation procedure can be found in the review paper and the recent book by Tryggvason et al. [10,33]. We have introduced some modifications in the standard procedure for handling certain quantities which are discussed in the relevant sections.

Also, to keep the front resolution within the prescribed limits, front restructuring is necessary. The element addition and deletion is performed using a third-order Legendre polynomial fit to preserve interface curvature during the restructuring [10]. Interface location is updated at each time step by moving the individual marker points; the velocity of each marker point comprises of the local flow velocity and the velocity of vaporization, i.e.,

$$\frac{d\mathbf{x}_\Gamma}{dt} = u_n \mathbf{n}_\Gamma, \quad (16)$$

where

$$u_n = \frac{1}{2} (\mathbf{u}_l + \mathbf{u}_g) \cdot \mathbf{n} - \frac{\dot{q}_\Gamma}{2h_{lg}} \left( \frac{1}{\rho_l} + \frac{1}{\rho_g} \right). \quad (17)$$

Further details of the front-tracking method are available in a paper by Unverdi and Tryggvason [9] and a review by Tryggvason et al. [10].

### 3.1. Flow solver

The flow equations are solved on an Eulerian grid using the projection method developed by Chorin [34]. It is a predictor–corrector type method in which we first predict the temporary velocity field by ignoring the pressure effects, and in the second step, the predicted velocity field is corrected to satisfy the continuity equation, Eq. (2). The momentum equations can be written in the form:

$$\frac{\rho^{n+1} \mathbf{u}^{n+1} - \rho^n \mathbf{u}^n}{\Delta t} = \mathbf{A}^n - \nabla p, \quad (18)$$

where  $\mathbf{A}$  represents the advection, the diffusion, the gravitational and the surface tension force terms and the superscript  $n$  indicates the current time level. The projection method splits the above equation as

$$\frac{\rho^{n+1} \mathbf{u}^* - \rho^n \mathbf{u}^n}{\Delta t} = \mathbf{A}^n, \quad (19)$$

$$\frac{\rho^{n+1} \mathbf{u}^{n+1} - \rho^{n+1} \mathbf{u}^*}{\Delta t} = -\nabla p, \quad (20)$$

where  $\mathbf{u}^*$  is the unprojected velocity field, calculated using Eq. (19), by ignoring the pressure effects. Next, we take divergence of Eq. (20) to obtain a Poisson equation for the pressure, i.e.,

$$\nabla \cdot \frac{1}{\rho^{n+1}} \nabla p = \frac{\nabla \cdot \mathbf{u}^* - \nabla \cdot \mathbf{u}^{n+1}}{\Delta t}. \quad (21)$$

For  $\nabla \cdot \mathbf{u}^{n+1}$ , we use Eq. (2) as

$$\nabla \cdot \mathbf{u}^{n+1} = \frac{1}{h_{lg}} \left( \frac{1}{\rho_g} - \frac{1}{\rho_l} \right) \left[ \int_A \delta(\mathbf{x} - \mathbf{x}_\Gamma) \dot{q}_\Gamma dA_\Gamma \right]^{n+1}, \quad (22)$$

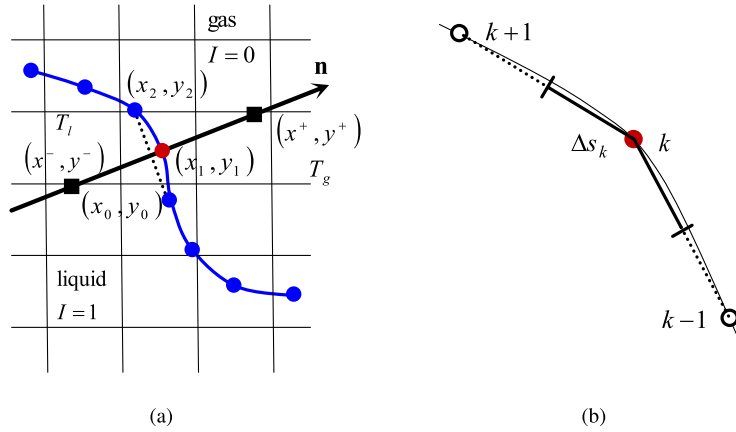


**Fig. 2.** (a) The method used to approximate the temperature gradients at the interface. (b) Computation of the interface length  $\Delta s_k$  corresponding to the  $k$ th marker point.

where  $\dot{q}_\Gamma$  is computed at  $(n+1)$  time level, i.e., using the front position at  $(n+1)$ . We substitute Eq. (22) into Eq. (21) and solve the resulting Poisson equation for pressure iteratively using a Red–Black Gauss–Seidel method with a Successive Over Relaxation (SOR). Once  $\mathbf{u}^*$  and  $p$  are known, the velocity field at the next time level,  $n+1$ , is found using Eq. (20) as:

$$\mathbf{u}^{n+1} = \mathbf{u}^* - \frac{\Delta t}{\rho^{n+1}} \nabla p. \quad (23)$$

The above algorithm is first order accurate in time. However, it can easily be extended for the second-order accuracy using a predictor corrector scheme as described by Tryggvason et al. [10,24].

### 3.2. Temperature gradient based evaporation model

In this model, it is assumed that the interface temperature  $T^\Gamma$  is the same as the saturation temperature  $T_{sat}$ , since pressure fluctuations in the system are small as compared to the absolute pressure. Thus the energy jump condition, Eq. (7), is used to calculate the heat flux per unit time at the interface, and is rewritten here for the  $k$ th marker point as

$$\dot{q}_{\Gamma_k} = k_g \left. \frac{\partial T}{\partial n} \right|_g^{\Gamma_k} - k_l \left. \frac{\partial T}{\partial n} \right|_l^{\Gamma_k}, \quad (24)$$

where  $\Gamma_k$  represents the  $k$ th marker point of the interface. A first-order one-sided finite difference discretization of Eq. (24) yields [24,36]

$$\dot{q}_{\Gamma_k} = \frac{1}{\eta h} [k_g(T_g - T_{sat}) - k_l(T_{sat} - T_l)], \quad (25)$$

where  $T_g$  and  $T_l$  are the temperatures approximated at points  $(x^+, y^+)$  and  $(x^-, y^-)$ , in the gas and the liquid domains, respectively, using a bi-linear interpolation, as shown in Fig. 2(a). These points are at a distance  $\eta h$ , normal from the  $k$ th marker point  $(x_1, y_1)$ . In Eq. (25),  $h$  is the uniform grid spacing and  $\eta$  scales the length of the probe and can be selected between 1–2 without any significant effect on the results [23,24,28]. Once  $\dot{q}_{\Gamma_k}$  is found, the last term of the energy equation, Eq. (5), is computed first and then smoothed onto the neighbouring fixed grid nodes in a conservative manner. Following Tryggvason et al. [10,33], for smoothing an interface quantity, say  $\phi_\Gamma$ , onto fixed grid node  $(i, j)$  in two-dimensions, we must have

$$\int_{\Delta s} \phi_\Gamma(s) ds = \int_{\Delta A} \phi_{i,j}(\mathbf{x}) dA, \quad (26)$$

which is approximated as

$$\phi_{i,j} = \sum_k \phi_\Gamma^k w_{i,j}^k \frac{\Delta s_k}{h^2}, \quad (27)$$

where  $\Delta s_k$  is the length of the piece of the interface between the centers of the front elements sharing the  $k$ th marker point and is calculated as shown by the thick lines in Fig. 2(b); and  $w_{i,j}^k$  is the weight of the fixed grid node  $(i, j)$  corresponding to the  $k$ th marker point and is calculated using the Peskin's cosine function [37]. The weights must also satisfy the consistency condition

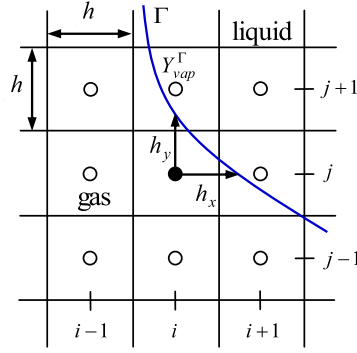


Fig. 3. Schematic illustration of an interface cell showing the nomenclature.

$$\sum_{i,j} w_{i,j}^k = 1. \quad (28)$$

Next, for the species field, we need  $\dot{m}_{\Gamma_k}$ , which can be computed as,

$$\dot{m}_{\Gamma_k} = \frac{\dot{q}_{\Gamma_k}}{h_{lg}}. \quad (29)$$

### 3.3. Species gradient based evaporation model

In this model, species concentration gradient at the interface is the only driving force for the phase change. The species mass fraction at the interface and consequently the evaporative mass flux is computed using the Clausius–Clapeyron relation. For the  $k$ th marker point of the interface, the evaporative mass flux per unit time ( $\dot{m}_{\Gamma_k}$ ) is computed using Eq. (9) as

$$\dot{m}_{\Gamma_k} = \frac{\rho_g D \alpha \frac{\partial Y}{\partial n} \Big|_{\Gamma_k}^g}{1 - Y_{vap}^{\Gamma_k}}, \quad (30)$$

where  $Y_{vap}^{\Gamma_k}$  is obtained from the Clausius–Clapeyron relation, i.e., Eqs. (10)–(11). The species gradient in the gas phase, normal to the interface, is calculated following the same procedure as discussed for the temperature gradient (see Fig. 2a). Corresponding to each marker point, we find a point  $(x^+, y^+)$  in the gas phase, at a distance  $\eta h$  normal from the marker point. The species mass fraction,  $Y^+$ , is approximated at  $(x^+, y^+)$  using a bi-linear interpolation. The species gradient is then calculated using a first-order one-sided finite difference approximation as

$$\frac{\partial Y}{\partial n} \Big|_{\Gamma_k}^g = \frac{1}{\eta h} (Y_{vap}^{\Gamma_k} - Y^+). \quad (31)$$

To solve the governing equation for the species mass fraction, the vapor mass fraction at the interface  $Y_{vap}^{\Gamma_k}$  may be applied directly as the boundary condition [38,39] or the mass flux per unit time  $\dot{m}_{\Gamma_k}$  can be distributed in a conservative manner onto a thin layer just outside the liquid droplet [30,31] and then added as a source term to the species equation. Both the strategies are briefly described below.

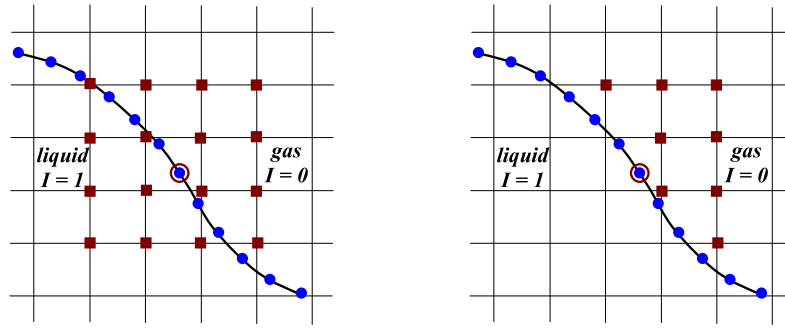
#### 3.3.1. Interface mass fraction as the Dirichlet boundary condition

In this case, the interface mass fraction,  $Y_{vap}^{\Gamma_k}$ , is applied as the Dirichlet boundary condition. The first step is to identify the grid cells which contain interface in their immediate vicinity. An algorithm is devised to find the interface cells based on the indicator function  $I$ , which defines interface as  $I = 0.5$ . An array is defined to store interface cells coordinates and is updated at each time step.

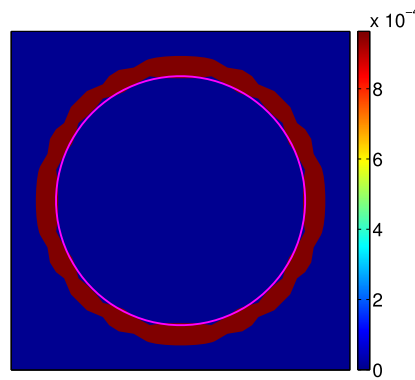
The discretization of convective and diffusive terms of the species equation, Eq. (6), is modified in the interface cells to incorporate  $Y_{vap}^{\Gamma_k}$  as the boundary condition. Fig. 3 shows one of the several irregular stencil configurations that may arise depending on the interface location. The convective term is approximated using a first-order upwind scheme [39]. A second order central difference discretization of the diffusion term for the interface cell  $(i, j)$  in Fig. 3 can be written as

$$(D_\alpha \nabla \cdot \nabla Y)_{i,j} = D_{\alpha(i,j)} \left( \frac{\partial^2 Y}{\partial x^2} + \frac{\partial^2 Y}{\partial y^2} \right)_{i,j} \quad (32)$$

$$= D_{\alpha(i,j)} \left\{ \left( \frac{2Y_{i-1,j}}{h(h+h_x)} - \frac{2Y_{i,j}}{h(h_x)} + \frac{2Y_{vap}^{\Gamma_k}}{h_x(h+h_x)} \right) + \left( \frac{2Y_{i,j-1}}{h(h+h_y)} - \frac{2Y_{i,j}}{h(h_y)} + \frac{2Y_{vap}^{\Gamma_k}}{h_y(h+h_y)} \right) \right\}, \quad (33)$$



(a) The conventional symmetric distribution stencil. (b) The modified one-sided distribution stencil.



(c) Evaporative mass source distributed outside the droplet.

**Fig. 4.** Treatment of the evaporation mass flux per unit time  $\dot{m}_{\Gamma_k}$  as a source term: schematic plot showing (a) the standard symmetric distribution stencil and (b) its modified version. Subfigure (c) is the contour plot of vapor mass fraction showing the distribution of  $\dot{m}_{\Gamma_k}$  onto the fixed Eulerian grid using modified strategy for a static evaporating droplet case; the convective and diffusive terms of species equation are switched off to better explain the scenario. (For interpretation of the colors in this figure, the reader is referred to the web version of this article.)

where  $h$  is the uniform grid size;  $h_x$  and  $h_y$  are the distances between cell center  $(i, j)$  and the interface in  $x$  and  $y$  directions, respectively. In the rest of the domain, discretization of the species equation is fairly straight forward.

### 3.3.2. Evaporation mass flux as a source term

Instead of applying  $Y_{vap}^{\Gamma_k}$  as the Dirichlet boundary condition, the evaporation mass flux per unit time,  $\dot{m}_{\Gamma_k}$ , found using Eq. (30), is distributed as a species source,  $\dot{S}_\alpha$ , onto the adjacent fixed grid nodes, just outside the interface, in a conservative manner. The conventional symmetric and the modified one-sided distribution stencils are schematically depicted in Figs. 4(a) and 4(b), respectively. This approach is similar and closely related to the adsorption layer concept developed by Muradoglu and Tryggvason [30,31] for the treatment of mass exchange between the interface and bulk fluid in the simulation of soluble surfactant in multiphase flows. The species equation, Eq. (6), is thus modified to account for the evaporative mass transfer as a source term

$$\frac{\partial Y_\alpha}{\partial t} + \mathbf{u} \cdot \nabla Y_\alpha = \nabla \cdot D_\alpha \nabla Y_\alpha + \frac{\dot{S}_\alpha}{\rho} \quad \alpha = 1, 2, \dots, n_s. \quad (34)$$

The source term  $\dot{S}_{\alpha i,j}$  at grid node  $(i, j)$  is approximated as [10,33]

$$\dot{S}_{\alpha i,j} = \sum_k \dot{m}_{\Gamma_k} w_{i,j}^k \frac{\Delta s_k}{h^2}, \quad (35)$$

where  $\dot{m}_{\Gamma_k}$  is evaporation mass flux per unit time computed at the  $k$ th marker point,  $\Delta s_k$  is the length of the interface corresponding to the  $k$ th marker point (see Fig. 2b),  $h$  is the uniform grid spacing and  $w_{i,j}^k$  is the weight of grid point  $(i, j)$ . The weight should satisfy the consistency condition in order to conserve the total source strength in going from the interface to the grid, i.e.,



$$\sum_i \sum_j w_{i,j}^k = 1. \quad (36)$$

The weight for the grid node  $(i, j)$ , for smoothing a quantity from the  $k$ th marker point, can be written as

$$w_{i,j}^k = \frac{\tilde{w}_{i,j}^k}{\sum_i \sum_j \tilde{w}_{i,j}^k}. \quad (37)$$

The non-normalized weight is obtained as a product of one-dimensional distribution functions, i.e.,

$$\tilde{w}_{i,j}^k = d(x_{\Gamma_k} - ih)d(y_{\Gamma_k} - jh), \quad (38)$$

where  $(x_{\Gamma_k}, y_{\Gamma_k})$  is the coordinate of the  $k$ th marker point and the distribution function  $d$  is a slightly modified version of the Peskin's cosine function [30,31,37] defined as

$$d(x) = \begin{cases} \frac{1}{2\lambda} \left(1 + \cos\left(\frac{\pi x}{\lambda}\right)\right) & \text{if } |x| < \lambda \text{ and } I < 0.5, \\ 0 & \text{otherwise,} \end{cases} \quad (39)$$

where  $\lambda$  is the width of the layer onto which  $\dot{m}_{\Gamma_k}$  is distributed as a mass source, and is selected as  $\lambda = 2h$  in the present study. We also checked for  $\lambda = 3h$  but no considerable effect on the output parameters is observed. Fig. 4(c) shows the sample contour plot of the species mass source smoothed onto the fixed grid following the above strategy, i.e.,  $I < 0.5$ .

### 3.4. Overall solution procedure

The overall solution procedure is briefly outlined below:

- i. Heat and mass fluxes per unit time,  $\dot{q}_{\Gamma}^n$  and  $\dot{m}_{\Gamma}^n$ , are computed using temperature and species fields at time level  $n$ , using Eq. (7) and Eq. (9), respectively.
- ii.  $\dot{q}_{\Gamma}^n$  is distributed onto the fixed grid using the Peskin's distribution function [37].
- iii. The procedure described in section 3.3.1 or 3.3.2 is used to handle the species mass fraction boundary condition at the interface.
- iv. Interface is advected for the next time level,  $n + 1$ , by simply integrating Eq. (16) as  $\mathbf{x}_{\Gamma}^{n+1} = \mathbf{x}_{\Gamma}^n + \Delta t u_n \mathbf{n}_{\Gamma}$ , where  $u_n$  is computed using Eq. (17).
- v. Indicator function at new interface position,  $I^{n+1}$ , is calculated based on the new interface location,  $\mathbf{x}_{\Gamma}^{n+1}$ .  $(\rho c_p)^{n+1}$  field is also updated based on the new indicator function, i.e.,  $I^{n+1}$ .
- vi. The energy (Eq. (5)) and species (Eq. (6) or (34)) equations are solved for the new temperature  $T^{n+1}$  and species  $Y^{n+1}$  fields, respectively.
- vii.  $\dot{q}_{\Gamma}^{n+1}$  is calculated and distributed onto the fixed grid following the steps i–ii.
- viii. Next, we solve the flow equations for the new velocity field,  $\mathbf{u}^{n+1}$ , as discussed in Section 3.1. We need the surface tension term while solving Navier–Stokes equation. We compute the surface tension for each front element at the interface location,  $\mathbf{x}_{\Gamma}^n$ , and distribute it onto the neighboring fixed grid nodes using the Peskin's distribution function [37].
- ix. The material property fields are updated for the time level  $n + 1$  using Eq. (15).
- x. Restructure the Lagrangian interface grid at each time step to keep the front element size within the prespecified limits.

## 4. Results and discussion

### 4.1. Temperature gradient based evaporation model

This model simulates the evaporative multiphase systems where the temperature gradient at the interface drives the phase change, e.g., the fuel droplet evaporation and burning in the internal combustion engines.

#### 4.1.1. Validation test – 1: the Stefan problem

The Stefan problem is a well-known test case to validate the phase change models [12,14,15,18,23,24,40]. Fig. 5 shows the schematic of the Stefan problem used in this study. A vertical interface separates the liquid and the vapor phases. Both the phases are assumed to be incompressible and are initially at rest at the saturation temperature condition,  $T_{sat}$ . The temperature of the left wall,  $T_w$ , adjacent to the vapor phase, is increased above the saturation temperature. The heat flows from the wall towards the interface. At the interface, the liquid vaporizes due to the temperature gradient. The interface moves towards right due to the free flow boundary conditions applied at the right boundary. As a result, a velocity field is also developed in the liquid phase. However, the liquid temperature stays fixed at the saturation value. The vapor is assumed to remain stationary, therefore, diffusion is responsible for heat transfer from the wall to the interface. Hence, the energy equation needs to be solved just in the vapor phase and can be written as

$$\frac{\partial T}{\partial t} = \alpha_g \frac{\partial^2 T}{\partial x^2} \quad 0 \leq x \leq x_{\Gamma}(t), \quad (40)$$

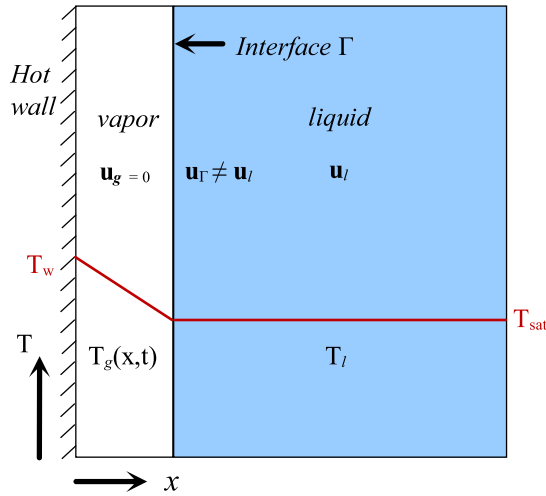


Fig. 5. Schematic of the Stefan problem.

where  $T$  is the temperature,  $\alpha_g$  is the thermal diffusivity of the vapor phase and  $x_\Gamma(t)$  is the interface location at time  $t$ . Equation (40) is solved subject to the boundary conditions

$$T(x=0, t) = T_w, \quad T(x=x_\Gamma(t), t) = T_{sat}. \quad (41)$$

Heat flux per unit time at the interface,  $\dot{q}_\Gamma$ , is computed using the energy jump condition

$$\dot{q}_\Gamma = k_g \left. \frac{\partial T}{\partial n} \right|_g, \quad (42)$$

where  $k_g$  is the thermal conductivity of the vapor phase. The analytical solution for the interface location at any time  $t$  can be expressed as

$$x_\Gamma(t) = 2\beta\sqrt{\alpha_g t}, \quad (43)$$

where  $\beta$  is the solution of the transcendental equation

$$\beta \exp(\beta^2) \operatorname{erf}(\beta) = \frac{c_{p,g}(T_w - T_{sat})}{h_{lg}\sqrt{\pi}}. \quad (44)$$

The analytical value of temperature at any point  $x$  in the vapor domain and at any time instant  $t$  is given by the expression

$$T_g(x, t) = T_w + \left( \frac{T_{sat} - T_w}{\operatorname{erf}(\beta)} \right) \operatorname{erf}\left( \frac{x}{2\sqrt{\alpha_g t}} \right). \quad (45)$$

The velocity in the liquid phase can be found analytically using the following relation

$$u_l = \left( 1 - \frac{\rho_g}{\rho_l} \right) u_n, \quad (46)$$

where  $u_n = \beta\sqrt{\alpha_g/t}$ . For a flat interface with uniform velocity field, the momentum jump condition in the normal direction, Eq. (4), simplifies to the following pressure jump relation

$$p_g - p_l = -\rho_g \left( 1 - \frac{\rho_g}{\rho_l} \right) u_n^2. \quad (47)$$

The fluid properties used in this numerical test case are:  $\rho_g = 0.5$ ,  $\rho_l = 2.5$ ,  $\mu_g = 0.007$ ,  $\mu_l = 0.098$ ,  $k_g = 0.0035$ ,  $k_l = 0.0015$ ,  $c_{p,g} = c_{p,l} = 1.0$  and  $h_{lg} = 100$ . Saturation temperature,  $T_{sat}$ , is set as 10 and wall temperature  $T_w = 12$  to achieve the Stefan number to be  $St = 0.02$ .

We performed numerical simulations on a  $1 \times 1$  domain. Results are presented for four different density ratios, i.e.,  $\gamma = \rho_l/\rho_g = 5, 10, 20$  and 40. Vapor phase density,  $\rho_g$ , is varied to achieve these values; the thermal diffusivity  $\alpha_g$  is also changed as a result. For all the cases, the initial interface location is set as  $x_\Gamma = 0.1$ , which corresponds to different initial times  $t_0(\gamma)$  depending on the density ratio ( $\gamma$ ). The initial temperature field is specified in the vapor phase using the analytical solution, Eq. (45), at the initial time  $t_0(\gamma)$ . First, a grid convergence study is performed for density ratio  $\gamma = 20$ . The results for interface location and temperature profile show that a  $64 \times 64$  grid resolution gives a very good match with the analytical results as shown in Fig. 6.

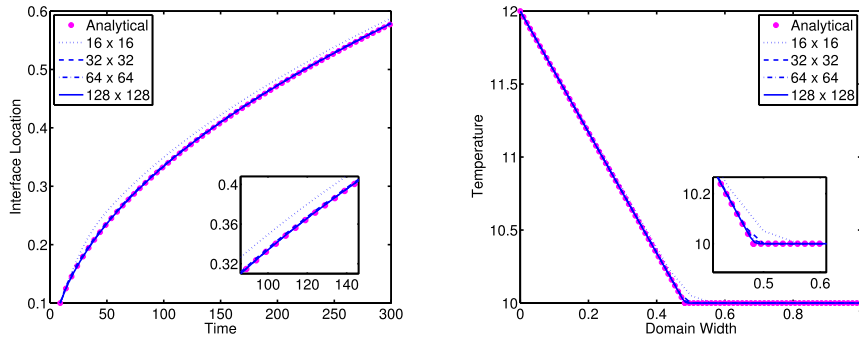


**Fig. 6.** Grid convergence results for the Stefan problem for density ratio  $\gamma = 20$ . (Left) the evolution of the interface location, (right) the temperature profile at  $t = 208.98$ . The insets show the enlarged views in each plot.

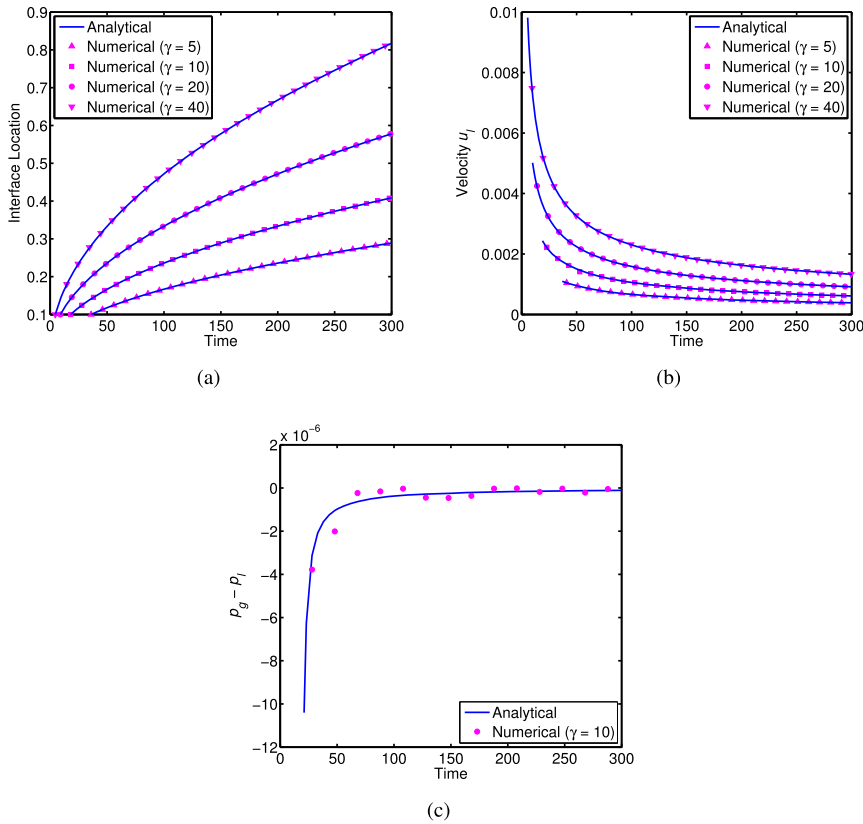


**Fig. 7.** Comparison of the analytical and numerical results for the 1D Stefan problem. The evolution of (a) the interface location, (b) the liquid phase velocity, and (c) the pressure difference with time. Grid:  $64 \times 64$ .

Next, the numerical results of interface location, liquid phase velocity and pressure jump are compared with the analytical solutions for different density ratios. A very good agreement is observed for all the cases, as shown in Fig. 7.

#### 4.1.2. Validation test – 2: The sucking interface problem

The sucking interface problem is also a benchmark case used to validate the temperature gradient based phase change model and has previously been studied by Welch and Wilson [12] and Guedon [40] to validate their phase change models. In this problem, a vapor layer is attached to the left wall of the domain while the rest is filled with a liquid as schematically shown in Fig. 8. Both phases are assumed to be incompressible and are separated by a vertical interface. The vapor phase is at saturation temperature  $T_{sat}$ , and stays at rest throughout the simulation. The liquid temperature  $T_{\infty}$  is higher than the saturation value, therefore, the phase change will occur at the interface. This will cause the interface to move towards right and a flow will be developed in the liquid phase. The heat of vaporization, absorbed at the interface due to phase change, comes from the liquid, which results in the formation of thermal boundary layer at the interface. A complete

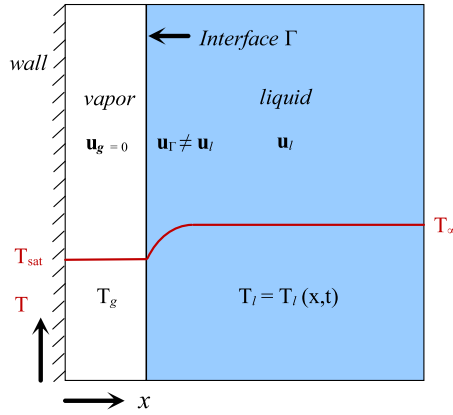


Fig. 8. Schematic of the sucking interface problem.

convection–diffusion energy equation needs to be solved in the liquid phase in the following form

$$\frac{\partial T}{\partial t} + \mathbf{u} \cdot \nabla T = \alpha_l \frac{\partial^2 T}{\partial x^2} \quad x_\Gamma(t) \leq x \leq 1, \quad (48)$$

subject to the boundary condition

$$T(x \leq x_\Gamma(t), t) = T_{sat}, \quad (49)$$

where  $\alpha_l$  is the thermal diffusivity of the liquid phase. Heat flux per unit time at the interface is computed using the energy jump condition given by Eq. (7). The sucking interface problem is a more stringent test case as compared to the Stefan problem since we need to solve the convective term of the energy equation coupled with the Navier–Stokes equations in addition to the diffusion term. Analytical solutions are available in the literature for this test problem [12,40]. At any time  $t$ , the interface location is calculated using the same expression as for the Stefan problem

$$x_\Gamma(t) = 2\beta\sqrt{\alpha_g t},$$

where  $\beta$  is the solution of the following transcendental equation

$$\exp(\beta^2) \operatorname{erf}(\beta) \left[ \beta - \frac{(T_\infty - T_{sat}) c_{p,g} k_l \sqrt{\alpha_g} \exp\left(-\beta^2 \frac{\rho_g^2 \alpha_g}{\rho_l^2 \alpha_l}\right)}{h_{lg} k_g \sqrt{\pi \alpha_l} \operatorname{erfc}\left(\beta \frac{\rho_g \sqrt{\alpha_g}}{\rho_l \sqrt{\alpha_l}}\right)} \right] = \frac{c_{p,g} (T_w - T_{sat})}{h_{lg} \sqrt{\pi}}. \quad (50)$$

The analytical solution for the temperature profile in the vapor phase is given as

$$T_g(x, t) = T_w + \left( \frac{T_{sat} - T_w}{\operatorname{erf}(\beta)} \right) \operatorname{erf}\left( \frac{x}{2\sqrt{\alpha_g t}} \right). \quad (51)$$

The temperature profile can be found in the liquid phase analytically using the following relation

$$T_l(x, t) = T_\infty - \left[ \frac{T_\infty - T_w}{\operatorname{erfc}\left(\beta \frac{\rho_g \sqrt{\alpha_g}}{\rho_l \sqrt{\alpha_l}}\right)} \right] \operatorname{erfc}\left( \frac{x}{2\sqrt{\alpha_l t}} + \frac{\beta(\rho_g - \rho_l)}{\rho_l} \sqrt{\frac{\alpha_g}{\alpha_l}} \right). \quad (52)$$

The horizontal velocity can be found in the liquid phase, at any time  $t$ , using the same expression as we used for the Stefan problem, Eq. (46). Similarly, the pressure jump can be calculated analytically for this case too, using the same expression as we used for the Stefan problem, i.e., Eq. (47).

The fluid properties considered for this numerical test case are:  $\rho_g = 0.25$ ,  $\rho_l = 2.5$ ,  $\mu_g = 0.007$ ,  $\mu_l = 0.098$ ,  $k_g = 0.0035$ ,  $k_l = 0.0015$ ,  $c_{p,g} = c_{p,l} = 10.0$  and  $h_{lg} = 100$ . The saturation temperature  $T_{sat}$  is set as 10, which is also the wall temperature  $T_w$ . The liquid is superheated with  $T_\infty = 12$ . The simulations are performed on a  $1 \times 1$  domain. The interface is initially placed at  $x = 0.1$  which corresponds to the initial time  $t_0 = 24.7$ . The temperature is initialized in the domain using the analytical solution, Eqs. (51) and (52). Numerical and analytical results of the interface location, temperature profile, liquid phase velocity and pressure jump are compared as shown in Fig. 9. The comparisons clearly show that the numerical results approach the analytical results as the grid is refined. Also, the numerical values of pressure jump satisfies the analytical values. Hence our implementation is grid convergent, tracks the interface very well and successfully captures the pressure jump and the sharp thermal boundary layer.

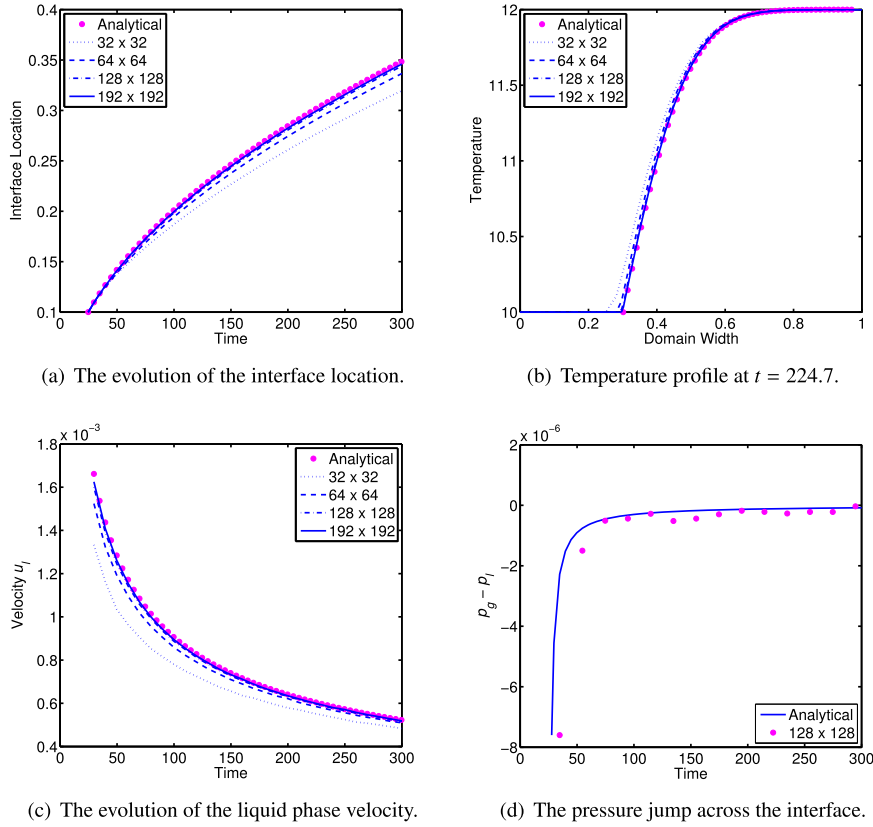


**Fig. 9.** Comparison of the numerical and analytical results for the sucking interface problem,  $\gamma = 10$ .

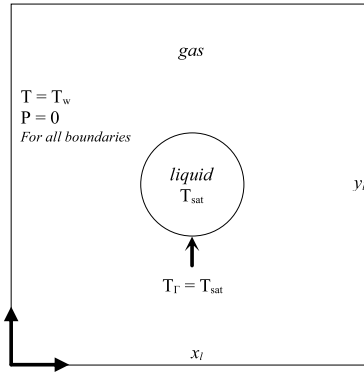


**Fig. 10.** The schematic illustration of a planar static droplet evaporation case.

#### 4.1.3. Evaporation of a two-dimensional static droplet

This case simulates the evaporation of a static droplet in a planar configuration.  $l_x$  and  $l_y$  denote the dimensions of the domain in the  $x$  and  $y$  coordinate directions with the origin marked at the bottom left corner as shown in Fig. 10. The same nomenclature is also used regarding the geometric dimensions of the domain in the rest of the study. A droplet of initial diameter  $d_o = 0.25$  mm is placed at the center of  $1 \times 1$  mm<sup>2</sup> domain ( $l_x = l_y$ ). At walls, the Dirichlet boundary condition is specified for temperature  $T_w$ ; and vapors are allowed to leave the domain freely. The physical properties considered here yield the non-dimensional parameters as  $\gamma = 5$ ,  $\zeta = 10$ ,  $Pr_l = 1.75$ ,  $Pr_g = 0.7$  and  $Sc = 1.0$ . The temperature inside the liquid droplet is initialized as  $T_{sat} = 373$  K and approximately stays constant during the simulation, whereas the temperature in the gaseous domain is higher than  $T_{sat}$ . This temperature gradient is varied to achieve various values of Stefan number,  $St$ . The length scale  $l_s$  and time scale  $t_s$  are selected as  $d_o$  and  $d_o^2/\alpha_g$ , respectively. Due to the temperature gradient at the interface, phase change occurs and a radially outward Stefan flow is generated in the gas domain. The area of the droplet,

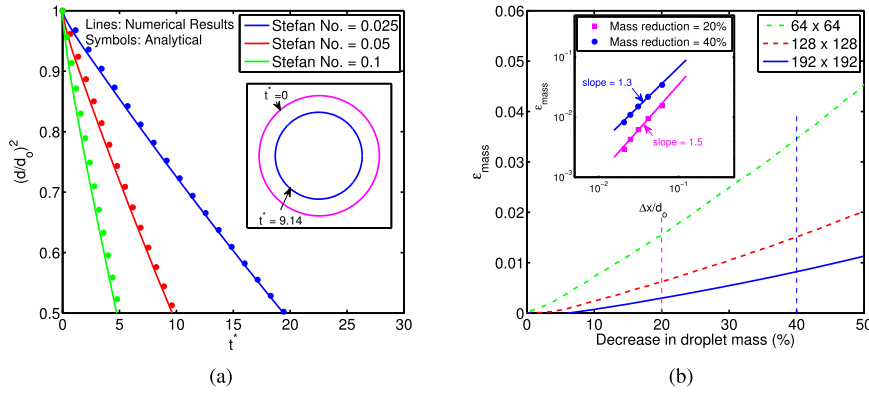


**Fig. 11.** (a) Comparison of the analytical and numerical results for the normalized  $d^2$  plotted versus time for  $St = 0.025, 0.05$  and  $0.1$ . The inset shows interface at two instants during evaporation at  $t^* = 0$  and  $9.14$ .  $St = 0.05$  and Grid:  $192 \times 192$ . (b) The mass conservation error is plotted for various grid resolutions showing the grid convergence as the grid is refined. The inset shows the order of accuracy of the method,  $St = 0.025$ . For both figures  $Sc = 1.0$ ,  $Pr_l = 1.75$ ,  $Pr_g = 0.7$ ,  $\gamma = 5$  and  $\zeta = 10$ .

and therefore the squared-diameter ( $d^2$ ) of a 2D evaporating droplet reduces with time according to the following analytical expression

$$\frac{dd^2}{dt} = -\frac{8k_g}{\rho_l c_{p,g}} \frac{\ln(1 + St)}{\ln(d_{ins}/\sqrt{d^2})}, \quad (53)$$

where  $d_{ins}$  is the diameter of the inscribed circle in the computational domain. We numerically integrated Eq. (53) using MATLAB ode45 solver and compared the time history of the normalized  $d^2$  with our simulation results for various values of Stefan number as shown in Fig. 11(a). A good agreement is observed till 50% of the droplet mass is evaporated for all the three cases. Also, it is observed that, doubling the Stefan number reduces the time to reach 50% mass reduction by half; the trend similar to the findings of Safari et al. [18]. The inset shows droplet interface at two time instants during the course of evaporation for  $St = 0.05$ . The spherical symmetry is perfectly maintained during the evaporation. A grid convergence study is performed for  $St = 0.025$ , the global mass conservation error being the target parameter. The global mass conservation error is defined as

$$\epsilon_{mass} = \left| \frac{\Delta M_l + \Delta M_{vap}}{M_{l_0}} \right|, \quad (54)$$

where  $\Delta M_l$  and  $\Delta M_{vap}$  denote the changes in the mass of the liquid droplet and in the vapor mass, respectively. These are computed as  $\Delta M_l = M_{l_0} - M_{l_t}$  and  $\Delta M_{vap} = M_{vap_0} - M_{vap_t}$ , where  $M_l$  and  $M_{vap}$  are the liquid and vapor masses, respectively. The subscript 'o' denotes the initial values and 't' represents the corresponding variables at time instant  $t$ . Fig. 11(b) shows the global mass conservation error plotted against the droplet mass reduction for various grid resolutions. The error approaches to zero as the grid is refined demonstrating the consistency and the grid convergence of our numerical method. The inset shows the order of convergence for this test case which is above the first order.

#### 4.1.4. Evaporation of a two-dimensional moving droplet

This is the case of an evaporating droplet moving under the action of the gravity. A droplet of initial diameter  $d_0 = 0.25$  mm is centered at  $(x_c, y_c) = (0.5, 3.6)$  mm in a  $1 \times 4$  mm<sup>2</sup> domain. The initial droplet temperature is  $T_{sat} = 373$  K whereas gas phase temperature is initialized as 480 K. Domain boundaries are specified as walls where the Dirichlet boundary conditions are specified for temperature and species mass fraction as  $T_w = 480.0$  K and  $Y_w = 0$ , respectively. The magnitude of the gravitational acceleration  $g$  is varied to obtain various combinations of Eotvos ( $EO$ ) and Morton ( $Mo$ ) numbers, which characterize the shape of drop moving in a surrounding fluid. Eotvos and Morton numbers are defined as  $EO = (\rho_l - \rho_g)d^2g/\sigma$  and  $Mo = \mu_g^4(\rho_l - \rho_g)g/\rho_g^2\sigma^3$ , respectively. The method is first tested for the global mass conservation and grid convergence for a moving droplet that deforms sufficiently while evaporating as may be the case in the combustion environment. The physical properties are selected to have the non-dimensional parameters as  $EO = 10$ ,  $Mo = 10 \times 10^{-4}$ ,  $St = 0.1$ ,  $Sc = 1$ ,  $Pr_l = 5.37$ ,  $Pr_g = 1.0$ ,  $\gamma = 5$  and  $\zeta = 20$ . The initial droplet diameter  $d_0$  is selected as the length scale and  $\sqrt{d_0/g}$  is the time scale for this case. Fig. 12 shows the contour plots of temperature and species mass fraction and the global mass conservation error for different grid resolutions. The results clearly indicate that the mass conservation error decreases as the grid is refined for this more stringent test case. Also the spatial order of accuracy is almost linear (1st-order). Fig. 13 shows the contour plots of species mass fraction for three separate cases, from left to right, in order of increasing droplet deformation. The corresponding  $EO$  and  $Mo$  numbers are  $(EO, Mo) = (5, 5 \times 10^{-4})$ ,  $(10, 10 \times 10^{-4})$  and  $(20, 20 \times 10^{-4})$ . The other parameters are fixed at  $St = 0.1$ ,  $Sc = 1$ ,  $Pr_l = 5.37$ ,  $Pr_g = 1.0$ ,  $\gamma = 5$  and  $\zeta = 20$  for all the three cases. It is observed that, as the droplet departs from a spherical shape, it evaporates faster. This trend is justified because

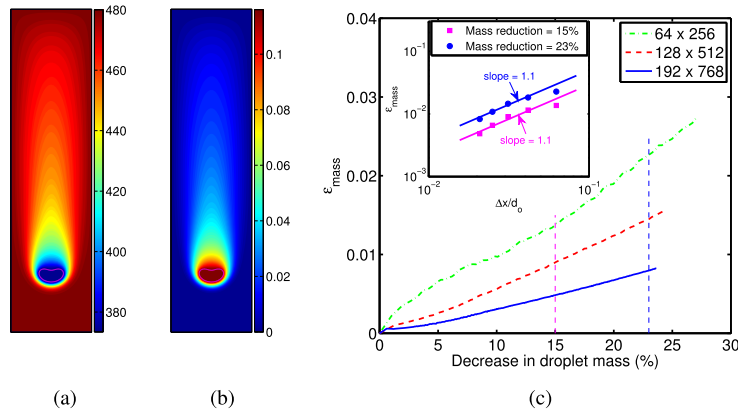


**Fig. 12.** The contour plots of (a) temperature and (b) species mass fraction for an evaporating droplet falling under the action of the gravity at  $t^* = 13.416$  and  $128 \times 512$  grid resolution. (c) The global mass conservation error is plotted for various grid resolutions showing the grid convergence. The inset shows the order of accuracy of the method.  $Eo = 10$ ,  $Mo = 10 \times 10^{-4}$ ,  $St = 0.1$ ,  $Sc = 1.0$ ,  $Pr_l = 5.37$ ,  $Pr_g = 1.0$ ,  $\gamma = 5$  and  $\zeta = 20$ . (For interpretation of the colors in this figure, the reader is referred to the web version of this article.)

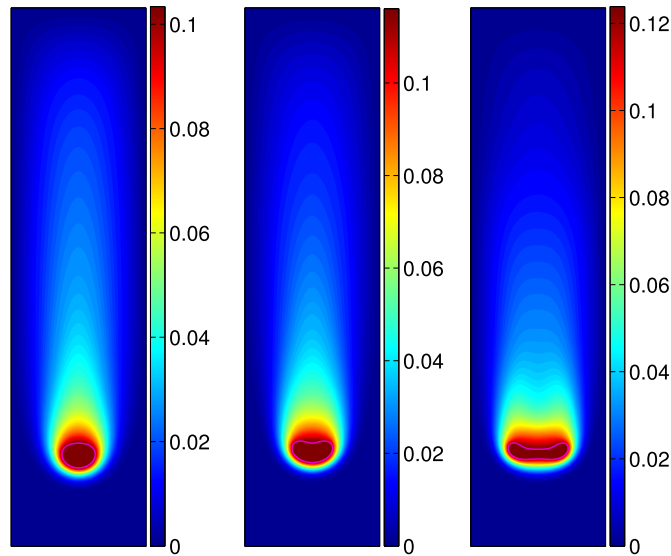


**Fig. 13.** Evaporation of droplets falling under gravity with varying degree of deformation. Contour plots of the species mass fraction for three separate cases (from left to right):  $Eo = 5$ ,  $Mo = 5 \times 10^{-4}$ ,  $t^* = 13.914$ ;  $Eo = 10$ ,  $Mo = 10 \times 10^{-4}$ ,  $t^* = 13.416$ ;  $Eo = 20$ ,  $Mo = 20 \times 10^{-4}$ ,  $t^* = 16.44$ . Grid:  $128 \times 512$ . (For interpretation of the colors in this figure, the reader is referred to the web version of this article.)

evaporation is a surface phenomenon and occurs due to temperature gradient at the interface; and since more surface area is exposed to high temperature in case of deformed droplets as compared to the spherical one, therefore, evaporation is enhanced.

#### 4.2. Species gradient based evaporation model

This model depicts a more general situation where phase change occurs owing to the species concentration gradient across the interface. A number of tests are performed to validate the numerical solution algorithm. The computation of evaporation mass flux is an important parameter which depends on the correct coupling of the interface temperature with the species mass fraction at the interface through the Clausius–Clapeyron relation. Also, the implementation of species boundary condition at the interface is very crucial for the species solver to ensure the global mass conservation.

##### 4.2.1. Validation test – 1: Evaporation mass flux

An efficient numerical phase change model must be able to predict evaporation mass flux accurately, since it is an important parameter in the phase change phenomenon that determines the rate of evaporation and consequently the interface location. The problem setup consists of a container filled with water up to a certain level. Air fills the rest of the container. The air–water interface is marked as  $y = 0$ . Based on the interface temperature, vapor mass fraction at the interface,  $Y_{vap}^\Gamma$ ,

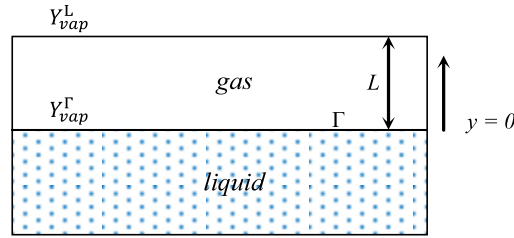


Fig. 14. A schematic illustration of the validation case for the evaporation mass flux.

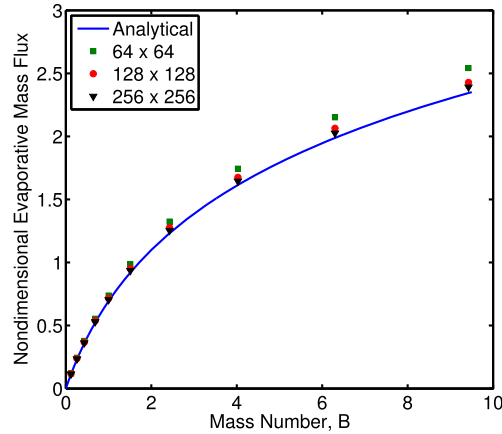


Fig. 15. Comparison of the numerical and the analytical non-dimensional evaporation fluxes for various values of mass number  $B$ .

is computed using the Clausius–Clapeyron relation. Sufficiently far from the interface, at  $y = L$ , the air is dry, i.e.,  $Y_{vap}^L = 0$ . At the interface, water vapor diffuses into the air and a Stefan flow is setup in the gas phase that convects the vapor away from the interface. Hence, a complete convective–diffusive species equation needs to be solved for the vapor field in the gas domain. The water is assumed to be motionless. The schematic of this test case is shown in Fig. 14. For this simplified test case, the interface temperature is assumed to stay constant during the simulation, therefore  $Y_{vap}^\Gamma$  is constant too. Also, it is assumed that the liquid evaporated is replenished exactly and continuously, therefore the location of the interface stays fixed. Furthermore, the surrounding gas is assumed to be insoluble in water so there is no net transport of surrounding gas into the container. The physical properties of water and air are used for this test case. For one complete simulation where interface temperature stays constant, these physical properties are also assumed to be constant, but for different interface temperature boundary conditions, the properties are varied accordingly.

The mass conservation principle applied over a small control volume for vapor source yields the following differential equation [41],

$$\dot{m}_{vap} = \dot{m}_{vap} Y_{vap} - \rho_g D_\alpha \left. \frac{dY_{vap}}{dy} \right|_\Gamma^g, \quad (55)$$

where  $\dot{m}_{vap}$  is the evaporation flux per unit time at the interface. Equation (55) is solved subject to the following boundary conditions

$$Y_{vap}|_{y=0} = Y_{vap}^\Gamma, \quad Y_{vap}|_{y=L} = Y_{vap}^L, \quad (56)$$

which results in the analytical solution given by

$$\dot{m}_{vap} = \frac{\rho_g D_\alpha}{L} \ln(1 + B), \quad (57)$$

where  $B$  is the mass number given as

$$B = \frac{Y_{vap}^\Gamma - Y_{vap}^L}{1 - Y_{vap}^\Gamma}. \quad (58)$$

The evaporation mass flux per unit time is non-dimensionalized by the scaling factor  $\rho_g D_\alpha / L$ . An increase in the interface temperature increases  $Y_{vap}^\Gamma$  and therefore the mass number  $B$  is also increased since  $Y_{vap}^L = 0$ . Fig. 15 compares the numerical results of the non-dimensional evaporation mass flux with the analytical solution for various values of mass number  $B$ .



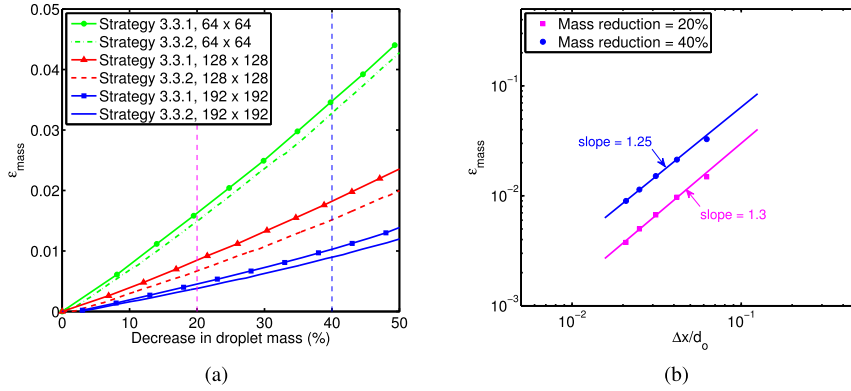


**Fig. 16.** (a) Comparison of the two strategies for implementing vapor mass fraction boundary condition at the interface. The global mass conservation error is plotted at various grid resolutions demonstrating the grid convergence. The strategy 3.3.2 shows lesser errors as compared to the strategy 3.3.1. (b) The global mass error is plotted against the normalized grid sizes for 20% and 40% droplet mass evaporation for strategy 3.3.2 displaying the spatial order of accuracy greater than 1. DBT = 313 K and RH = 10%.

The computational results approach the analytical solution as the grid is refined, which shows that our model is grid convergent and precisely computes the convective and diffusive mass transfer components. For high values of mass number  $B$ , i.e., high evaporation rates, much finer grid resolutions are required to reach the analytical values which is expected and self explanatory.

#### 4.2.2. Validation test – 2: Temperature comparison with psychrometric chart values

For this test case, the computational setup consists of a liquid droplet of initial diameter  $d_o = 0.25$  mm held stationary at the center of a  $1 \times 1$  mm<sup>2</sup> domain. Initially, the temperature (dry bulb temperature) is the same throughout the domain and the phase change occurs due to the species gradient at the interface resulting in a low temperature at the interface. This goes lower and lower as evaporation proceeds until a steady state temperature condition is attained at the interface, called the wet bulb temperature. The liquid droplet also comes into equilibrium with the wet bulb temperature. This wet bulb temperature is a function of the dry bulb temperature (DBT) and the relative humidity (RH) in the air. The Dirichlet boundary conditions are specified at the domain boundaries for both the temperature and the vapor mass fraction, i.e.,  $T_g$  and  $Y_{vap}$ , respectively.  $Y_{vap}$  can be computed as  $Y_{vap} = \omega_h / (1 + \omega_h)$ , where  $\omega_h$  is the humidity ratio which is a function of dry-bulb temperature and relative humidity; and can be read from a psychrometric chart. At the interface, the vapor mass fraction boundary condition  $Y_{vap}^\Gamma$  may be specified using any of the strategies discussed in Sections 3.3.1 or 3.3.2. Both of these are first compared for the global mass conservation for the case with DBT = 313 K and RH = 10%. The physical properties of air and water are used for all the following cases unless otherwise stated except for the liquid density  $\rho_l$  which is taken as 10 kg/m<sup>3</sup>.  $k_l$  is modified accordingly to obtain the thermal diffusivity value  $\alpha_l$  for water.  $d_o$  and  $d_o^2/D_\alpha$  are selected as the length and the time scales, respectively, for all the cases related to the static droplet evaporation. The comparison shown in Fig. 16(a) suggests that, for the same grid size, the adsorption layer concept of distributing mass flux in the immediate outer vicinity of the interface and then adding as source term (Section 3.3.2) results in better mass conservation as compared to directly imposing  $Y_{vap}^\Gamma$  as the interface boundary condition for species mass fraction (Section 3.3.1). However, for both the methods, the trends of global mass conservation error clearly show the grid convergence on grid refinement. Fig. 16(b) shows the global mass conservation error plotted against the non-dimensional grid size for the strategy 3.3.2. Two sets of data points are used corresponding to 20% and 40% mass losses during the droplet evaporation. The spatial order of accuracy is more than one in this case. For all the cases to follow, we stick with the strategy of Muradoglu and Tryggvason [30,31] (Section 3.3.2) for implementing vapor mass fraction boundary condition at the interface. Various cases are then simulated with dry bulb temperatures in the range 283 K–313 K and relative humidities 10–90%, and the resulting wet bulb temperatures are compared with the psychrometric chart values. A grid convergence study is performed first to select a suitable grid resolution applicable to the rest of the simulations. Fig. 17 shows the grid convergence results for the wet bulb temperature and the variation of squared-diameter ( $d^2$ ) with time corresponding to DBT = 283 K–313 K and RH = 10%. It is found that a  $128 \times 128$  grid resolution yields grid convergent results for both the indicators. Moreover, the temperature results converge faster as compared to the interface location. The results of the normalized  $d^2$  are also compared with the analytical solution. The analytical expression derived for the variation of  $d^2$  with time for a 2D evaporating droplet case is given by

$$\frac{dd^2}{dt} = -\frac{8\rho_g D_\alpha}{\rho_l} \frac{\ln(1+B)}{\ln(d_{ins}/\sqrt{d^2})}, \quad (59)$$

where  $B$  is defined by Eq. (58) and  $d_{ins}$  is the diameter of the inscribed circle in the computational domain. Equation (59) is solved using MATLAB ode45 solver. The analytical and numerical profiles for the variation of normalized  $d^2$  with time show

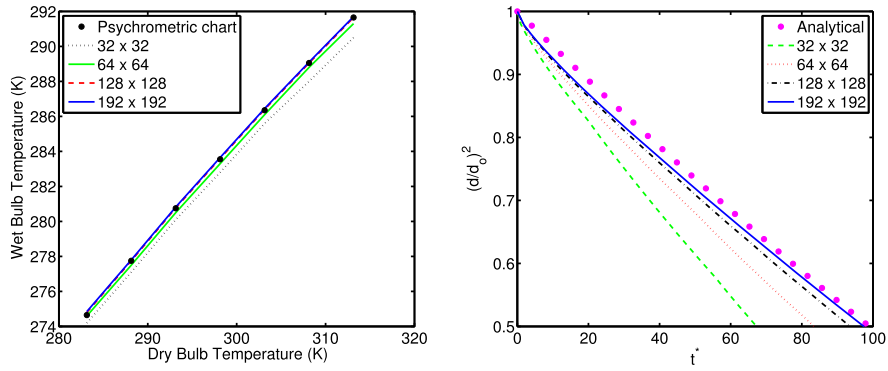


**Fig. 17.** Grid convergence study. (Left) Numerical results of wet bulb temperatures converge to the psychrometric chart values for DBT = 283 K–313 K and RH = 10%. (Right) The simulation results for the variation of normalized  $d^2$  with the non-dimensional time  $t^*$  compared with the analytical solution. DBT = 313 K, RH = 10%.

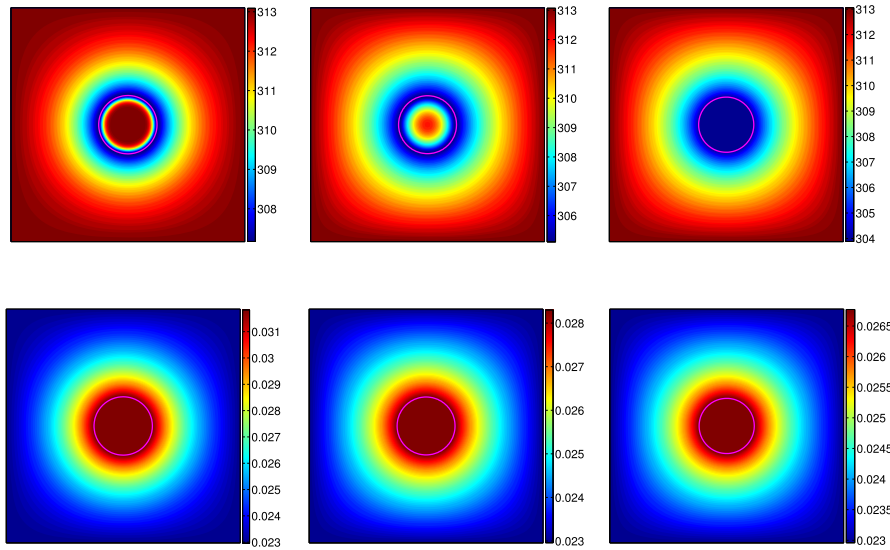


**Fig. 18.** Contour plots of temperature (top row) and species mass fraction (bottom row) for an evaporating droplet at non-dimensional times (from left to right)  $t^* = 0.424$ ,  $4.24$  and  $42.4$ ; the wet bulb temperature is reached in the right most plot of the top row. DBT = 313 K, RH = 50% and Grid:  $128 \times 128$ . (For interpretation of the colors in this figure, the reader is referred to the web version of this article.)

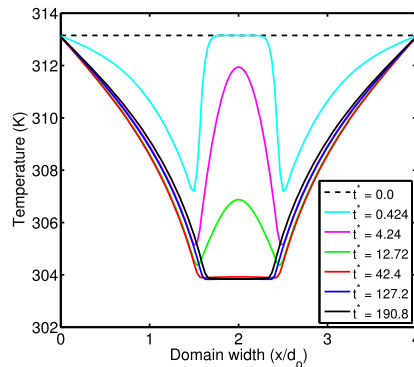


**Fig. 19.** Temperature profiles plotted along the horizontal center line of the domain width at various non-dimensional times  $t^*$ . The steady state temperature condition is achieved inside the evaporating droplet. DBT = 313 K, RH = 50%.

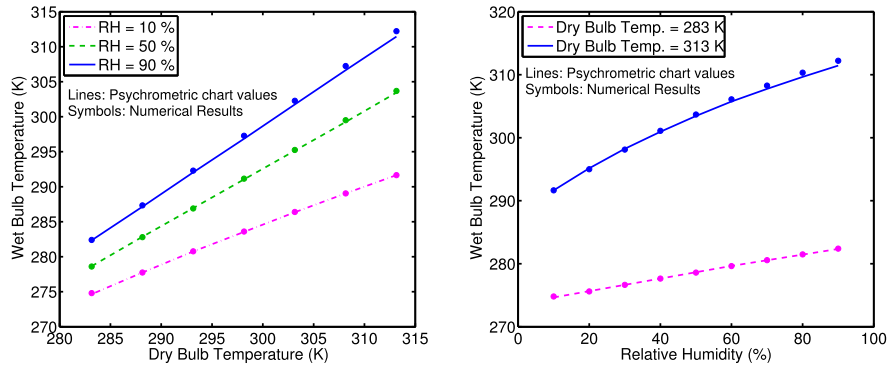


**Fig. 20.** Numerical results of wet bulb temperatures compared with the psychrometric chart values for various combinations of dry bulb temperatures and relative humidities. Grid:  $128 \times 128$ .

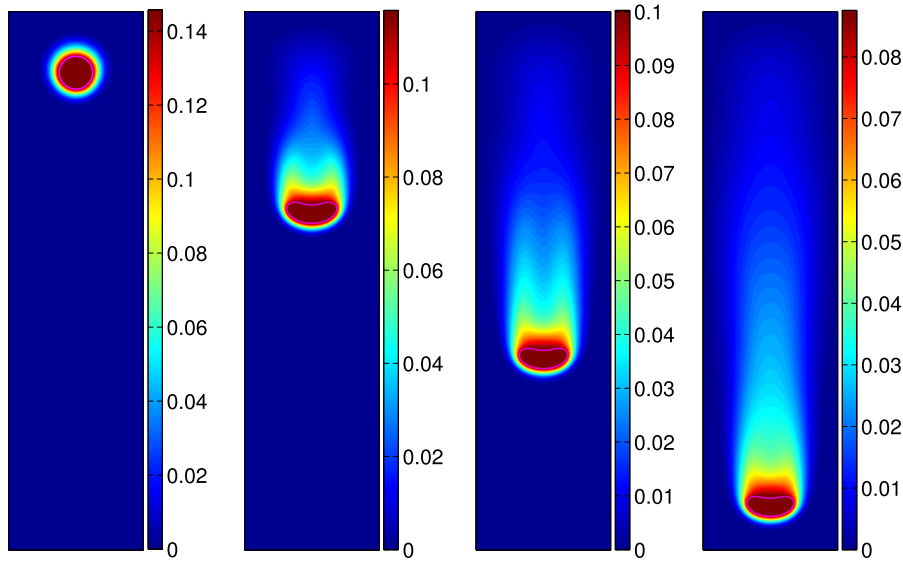


**Fig. 21.** Contour plots of the vapor mass fraction for a moving, deforming and evaporating droplet at four time instants  $t^* = 0.89, 5.37, 9.84$  and  $14.31$ . Grid:  $128 \times 512$ . The non-dimensional parameters are  $Eu = 10$ ,  $Mo = 10 \times 10^{-5}$ ,  $Sc = 1.0$ ,  $Pr_l = 54.08$ ,  $Pr_g = 0.15$ ,  $\gamma = 5$  and  $\zeta = 20$ . (For interpretation of the colors in this figure, the reader is referred to the web version of this article.)

good agreement as the grid is refined, as shown in Fig. 17. Some sample contour and line plots are then presented for the case with DBT = 313 K and RH = 50%. Fig. 18 shows the contour plots for the evolution of temperature and species mass fraction fields. A better illustration of the temperature evolution may be seen in Fig. 19, which shows temperature profiles along the horizontal center line of the domain at various time instants during the evaporation. Once an equilibrium wet bulb temperature is attained, all the heat absorbed just results in the phase change. Next, we made three sets of runs by keeping the relative humidity fixed at 10%, 50% and 90% respectively, and varying the dry bulb temperature in the range 283 K–313 K for each case. In the final batch of runs, the temperature is held constant at 283 K and 313 K and the relative humidity is varied from 10% to 90% for the each case. The comparison of the numerical results with the psychrometric chart results are shown in Fig. 20. Numerical results are in excellent agreement with the psychrometric chart values, however, some deviation is observed at high dry bulb temperatures and high relative humidities. This may be attributed to our constant properties assumption, since the thermophysical properties vary significantly at high temperatures and high relative humidities [42].

#### 4.2.3. Evaporating droplet falling under gravity

This section simulates the planar case of an evaporating droplet that moves due to the gravitational acceleration  $\mathbf{g}$ , and deforms during the journey. The initial diameter,  $d_0$ , of the droplet is 0.25 mm. The domain size is selected as  $1 \times 4 \text{ mm}^2$ . The droplet is initially placed with its center at (0.5, 3.6) mm and starts from the rest. Temperature is initialized as 371 K in the whole domain whereas the saturation temperature is  $T_{sat} = 373 \text{ K}$ . The domain boundaries are set as walls, and the Dirichlet boundary conditions are specified for the temperature and vapor mass fraction at walls as  $T_g = 371 \text{ K}$  and  $Y_{vap} = 0$ , respectively. The vapor mass fraction boundary condition at the interface is implemented following the strategy of Muradoglu and Tryggvason [30,31]. The other physical properties are selected to have the relevant non-dimensional

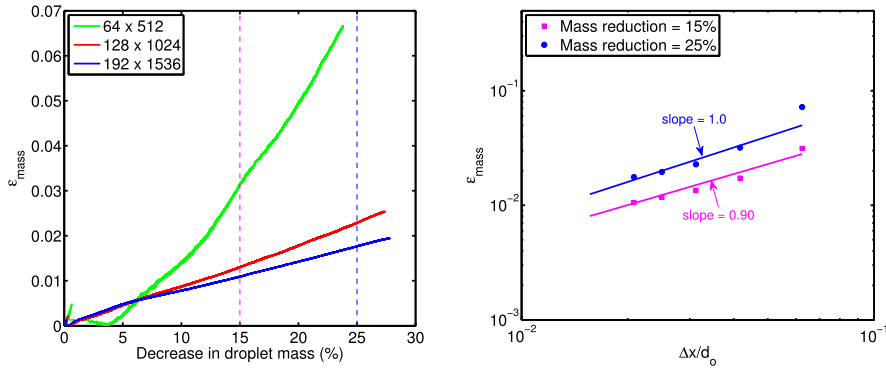


**Fig. 22.** (Left) The global mass conservation error for a moving deforming evaporating droplet at various grid resolutions. (Right) The global mass error versus the non-dimensional grid size after 15% and 25% loss in the droplet mass. The relevant nondimensional parameters are  $Eo = 10$ ,  $Mo = 10 \times 10^{-5}$ ,  $Sc = 1.0$ ,  $Pr_l = 54.08$ ,  $Pr_g = 0.15$ ,  $\gamma = 5$  and  $\zeta = 20$ .

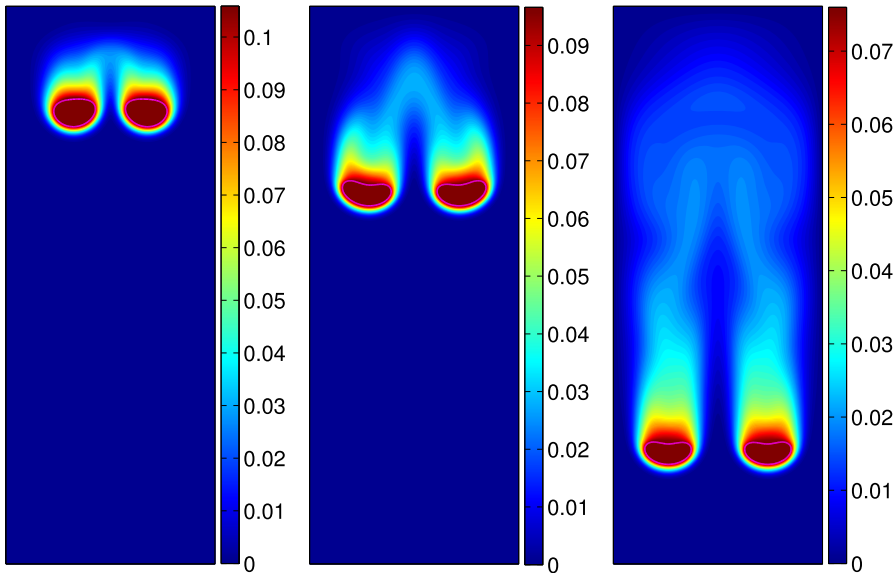


**Fig. 23.** Contour plots of the vapor mass fraction for two interacting droplets at various time instants ( $t^* = 2.68, 5.37$  and  $14.31$ ). The non-dimensional parameters are  $Eo = 10$ ,  $Mo = 10 \times 10^{-5}$ ,  $Sc = 1.0$ ,  $Pr_l = 54.08$ ,  $Pr_g = 0.15$ ,  $\gamma = 5$  and  $\zeta = 20$ . Grid:  $192 \times 512$ . (For interpretation of the colors in this figure, the reader is referred to the web version of this article.)

parameters as  $Eo = 10$ ,  $Mo = 10 \times 10^{-5}$ ,  $Sc = 1.0$ ,  $Pr_l = 54.08$ ,  $Pr_g = 0.15$ ,  $\gamma = 5$  and  $\zeta = 20$ .  $d_o$  and  $\sqrt{d_o/g}$  are the appropriate length  $l_s$  and time  $t_s$  scales, respectively; and the velocity scale is calculated as  $u_s = l_s/t_s$ . Fig. 21 shows the contour plots of the vapor mass fraction at different time instants during the life of droplet, as it falls due to the gravity. The global mass conservation results are shown in Fig. 22. It is observed that the global mass conservation error reduces as the grid is refined. The order of accuracy is close to one for this deformed droplet evaporation case which shows the ability of our method to handle highly deformed interfaces. The method is overall second order accurate in space but the spatial accuracy reduces to first order for the global mass conservation mainly due to the smoothing of discontinuous fields such as evaporation mass source at the interface.

Finally, some sample results are presented for the multiple droplets that move, evaporate, deform and interact with each other. Two droplets are initially placed with their centers  $2d_o$  apart in a  $1.5 \times 4 \text{ mm}^2$  domain and move under the action of the gravity. Temperature is initialized as 363 K in the whole domain whereas all other properties are same as for the single droplet case. Fig. 23 shows the snapshots of their path history as they start from the rest. The global mass conservation error plots are shown in Fig. 24.

## 5. Conclusions

A finite-difference/front-tracking method is developed to simulate the liquid–vapor phase change phenomenon. A one-field formulation is used to solve the governing equations on a fixed uniform Eulerian grid whereas the interface is

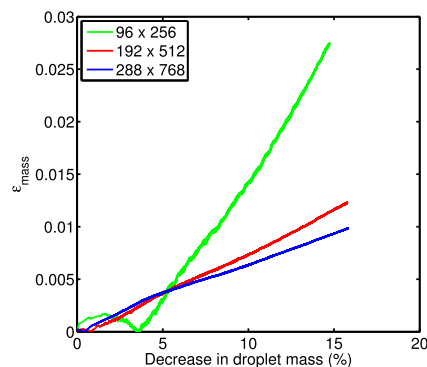


**Fig. 24.** The global mass conservation error plotted for two interacting and evaporating droplets at various grid resolutions. Error reduces as the grid is refined.

represented by a separate Lagrangian grid. Different interpolation and distribution schemes are used to communicate between these two grids. The Navier–Stokes equations are solved using a projection method, whereas the energy and species equations are solved in time using an explicit Euler method.

Both the temperature and the species gradient based phase change models are studied. The temperature gradient based model is validated against the benchmark cases, i.e., the Stefan and the sucking interface problems. Interface location, temperature profile and the liquid phase velocity are the parameters under investigation. Results are demonstrated to be grid convergent and are in excellent agreement with the analytical solutions. Two-dimensional static and moving droplet cases are then simulated in a planar configuration. For the static case, the global mass conservation and grid convergence studies are performed and very good results are obtained. The spherical symmetry of the droplet is maintained during the course of evaporation. Moving droplets take different shapes depending on the  $Eu$  and  $Mo$  numbers. Simulations are performed for the substantially deforming droplet cases and the numerical method is demonstrated to be grid convergent.

Species gradient based evaporation model employs the Clausius–Clapeyron equilibrium relation to compute species mass fraction at the interface and subsequently the evaporation mass flux. Species mass fraction boundary condition at the interface is implemented using two different strategies. The one that considers evaporative mass flux as a source term is found to be numerically efficient, easy to implement, gives better global mass conservation results and can easily be extended to 3D configuration. The numerical results of the non-dimensional evaporation mass flux is compared with the analytical solution for a simplified case and excellent agreement is observed on grid refinement. The global mass conservation and grid convergence checks are performed for a two-dimensional static droplet case. Results for both the indicators are excellent. In the steady state condition, the droplet temperature attains equilibrium with the air temperature at the interface, i.e., the wet bulb temperature, and can be read from a psychrometric chart. For various combinations of the dry bulb temperatures and relative humidities, the numerical results of wet bulb temperatures compare very well with the psychrometric chart values. Finally, simulations are performed for the highly deformed droplets falling in a gravitational field. Both single and two interacting droplets cases are studied. Global mass conservation is ensured for both the cases and mass conservation error converges to zero on grid refinement. We have observed that, for the novel species gradient based evaporation model, approximately 40% of the total computational time is utilized by the phase change solver for a static droplet evaporation case.

The current implementation is general and can easily be extended to incorporate more than one product species as is typically the case in droplet evaporation followed by a chemical reaction. This has application to a lot of real world engineering problems including fuel droplet evaporation and combustion in the internal combustion engines. It is also straightforward to extend the present numerical method to 3D geometries.

## Acknowledgements

The first author is supported by The Higher Education Commission of Pakistan. Computations are performed at HPC facility of the Koc University and TUBITAK-ULAKBIM HPC centre.

## References

- [1] F.H. Harlow, J.E. Welch, Numerical calculation of time dependent viscous incompressible flow of fluid with free surface, *Phys. Fluids* 8 (12) (1965) 2182–2189, <http://dx.doi.org/10.1063/1.1761178>.
- [2] C. Hirt, B. Nichols, Volume of fluid (VOF) method for the dynamics of free boundaries, *J. Comput. Phys.* 39 (1) (1981) 201–225, [http://dx.doi.org/10.1016/0021-9991\(81\)90145-5](http://dx.doi.org/10.1016/0021-9991(81)90145-5).
- [3] S. Osher, J.A. Sethian, Fronts propagating with curvature-dependent speed: algorithms based on Hamilton–Jacobi formulations, *J. Comput. Phys.* 79 (1) (1988) 12–49, [http://dx.doi.org/10.1016/0021-9991\(88\)90002-2](http://dx.doi.org/10.1016/0021-9991(88)90002-2).
- [4] M. Sussman, P. Smereka, S. Osher, A level set approach for computing solutions to incompressible two-phase flow, *J. Comput. Phys.* 114 (1) (1994) 146–159, <http://dx.doi.org/10.1006/jcph.1994.1155>.

- [5] D.M. Anderson, G.B. McFadden, A.A. Wheeler, Diffuse-interface methods in fluid mechanics, *Annu. Rev. Fluid Mech.* 30 (1) (1998) 139–165, <http://dx.doi.org/10.1146/annurev.fluid.30.1.139>.
- [6] D. Jacqmin, Calculation of two-phase Navier Stokes flows using phase-field modeling, *J. Comput. Phys.* 155 (1) (1999) 96–127, <http://dx.doi.org/10.1006/jcph.1999.6332>.
- [7] G. Ryskin, L.G. Leal, Numerical solution of free-boundary problems in fluid mechanics. Part 1. The finite-difference technique, *J. Fluid Mech.* 148 (1984) 1–17, <http://dx.doi.org/10.1017/S0022112084002214>.
- [8] J. Glimm, Nonlinear and stochastic phenomena: the grand challenge for partial differential equations, *SIAM Rev.* 33 (4) (1991) 626–643, <http://dx.doi.org/10.1137/1033137>.
- [9] S.O. Unverdi, G. Tryggvason, A front-tracking method for viscous, incompressible, multi-fluid flows, *J. Comput. Phys.* 100 (1) (1992) 25–37, [http://dx.doi.org/10.1016/0021-9991\(92\)90307-K](http://dx.doi.org/10.1016/0021-9991(92)90307-K).
- [10] G. Tryggvason, B. Bunner, A. Esmaeili, D. Juric, N. Al-Rawahi, W. Tauber, J. Han, S. Nas, Y.-J. Jan, A front-tracking method for the computations of multiphase flow, *J. Comput. Phys.* 169 (2) (2001) 708–759, <http://dx.doi.org/10.1006/jcph.2001.6726>.
- [11] M. Woerner, Numerical modeling of multiphase flows in microfluidics and micro process engineering: a review of methods and applications, *Microfluid. Nanofluid.* 12 (6) (2012) 841–886, <http://dx.doi.org/10.1007/s10404-012-0940-8>.
- [12] S.W. Welch, J. Wilson, A volume of fluid based method for fluid flows with phase change, *J. Comput. Phys.* 160 (2) (2000) 662–682, <http://dx.doi.org/10.1006/jcph.2000.6481>.
- [13] J. Schlottke, B. Weigand, Direct numerical simulation of evaporating droplets, *J. Comput. Phys.* 227 (10) (2008) 5215–5237, <http://dx.doi.org/10.1016/j.jcp.2008.01.042>.
- [14] G. Son, V. Dhir, Numerical simulation of film boiling near critical pressures with a level set method, *J. Heat Transf.* 120 (1) (1998) 183–192, <http://dx.doi.org/10.1115/1.2830042>.
- [15] F. Gibou, L. Chen, D. Nguyen, S. Banerjee, A level set based sharp interface method for the multiphase incompressible Navier Stokes equations with phase change, *J. Comput. Phys.* 222 (2) (2007) 536–555, <http://dx.doi.org/10.1016/j.jcp.2006.07.035>.
- [16] R.P. Fedkiw, T. Aslam, B. Merriman, S. Osher, A non-oscillatory Eulerian approach to interfaces in multimaterial flows (the ghost fluid method), *J. Comput. Phys.* 152 (2) (1999) 457–492, <http://dx.doi.org/10.1006/jcph.1999.6236>.
- [17] S. Tanguy, T. Menard, A. Berlemont, A level set method for vaporizing two-phase flows, *J. Comput. Phys.* 221 (2) (2007) 837–853, <http://dx.doi.org/10.1016/j.jcp.2006.07.003>.
- [18] H. Safari, M.H. Rahimian, M. Krafczyk, Extended lattice Boltzmann method for numerical simulation of thermal phase change in two-phase fluid flow, *Phys. Rev. E* 88 (2013) 013304, <http://dx.doi.org/10.1103/PhysRevE.88.013304>.
- [19] H. Safari, M.H. Rahimian, M. Krafczyk, Consistent simulation of droplet evaporation based on the phase-field multiphase lattice Boltzmann method, *Phys. Rev. E* 90 (2014) 033305, <http://dx.doi.org/10.1103/PhysRevE.90.033305>.
- [20] T. Lee, Effects of incompressibility on the elimination of parasitic currents in the lattice Boltzmann equation method for binary fluids, *Comput. Math. Appl.* 58 (5) (2009) 987–994, <http://dx.doi.org/10.1016/j.camwa.2009.02.017>.
- [21] D. Juric, G. Tryggvason, Computations of boiling flows, *Int. J. Multiph. Flow* 24 (3) (1998) 387–410, [http://dx.doi.org/10.1016/S0301-9322\(97\)00050-5](http://dx.doi.org/10.1016/S0301-9322(97)00050-5).
- [22] J. Qian, G. Tryggvason, C. Law, A front tracking method for the motion of premixed flames, *J. Comput. Phys.* 144 (1) (1998) 52–69, <http://dx.doi.org/10.1006/jcph.1998.5991>.
- [23] A. Esmaeili, G. Tryggvason, Computations of explosive boiling in microgravity, *J. Sci. Comput.* 19 (1) (2003) 163–182, <http://dx.doi.org/10.1023/A:1025347823928>.
- [24] A. Esmaeili, G. Tryggvason, Computations of film boiling. Part I: numerical method, *Int. J. Heat Mass Transf.* 47 (25) (2004) 5451–5461, <http://dx.doi.org/10.1016/j.ijheatmasstransfer.2004.07.027>.
- [25] A. Koyunov, J.G. Khinast, G. Tryggvason, Mass transfer and chemical reactions in bubble swarms with dynamic interfaces, *AIChE J.* 51 (10) (2005) 2786–2800, <http://dx.doi.org/10.1002/aic.10529>.
- [26] B. Aboulhasanzadeh, S. Thomas, M. Taeibi-Rahni, G. Tryggvason, Multiscale computations of mass transfer from buoyant bubbles, *Chem. Eng. Sci.* 75 (2012) 456–467, <http://dx.doi.org/10.1016/j.ces.2012.04.005>.
- [27] D. Juric, G. Tryggvason, A front-tracking method for dendritic solidification, *J. Comput. Phys.* 123 (1) (1996) 127–148, <http://dx.doi.org/10.1006/jcph.1996.0011>.
- [28] N. Al-Rawahi, G. Tryggvason, Numerical simulation of dendritic solidification with convection: two-dimensional geometry, *J. Comput. Phys.* 180 (2) (2002) 471–496, <http://dx.doi.org/10.1006/jcph.2002.7092>.
- [29] N. Al-Rawahi, G. Tryggvason, Numerical simulation of dendritic solidification with convection: three-dimensional flow, *J. Comput. Phys.* 194 (2) (2004) 677–696, <http://dx.doi.org/10.1016/j.jcp.2003.09.020>.
- [30] M. Muradoglu, G. Tryggvason, A front-tracking method for computation of interfacial flows with soluble surfactants, *J. Comput. Phys.* 227 (4) (2008) 2238–2262, <http://dx.doi.org/10.1016/j.jcp.2007.10.003>.
- [31] M. Muradoglu, G. Tryggvason, Simulations of soluble surfactants in 3d multiphase flow, *J. Comput. Phys.* 274 (2014) 737–757, <http://dx.doi.org/10.1016/j.jcp.2014.06.024>.
- [32] S. Nas, M. Muradoglu, G. Tryggvason, Pattern formation of drops in thermocapillary migration, *Int. J. Heat Mass Transf.* 49 (13–14) (2006) 2265–2276, <http://dx.doi.org/10.1016/j.ijheatmasstransfer.2005.12.009>.
- [33] G. Tryggvason, R. Scardovelli, S. Zaleski, *Direct Numerical Simulations of Gas–Liquid Multiphase Flows*, Cambridge University Press, 2011.
- [34] A.J. Chorin, Numerical solution of the Navier–Stokes equations, *Math. Comput.* 22 (1968) 745–762.
- [35] R. Borges, M. Carmona, B. Costa, W.S. Don, An improved weighted essentially non-oscillatory scheme for hyperbolic conservation laws, *J. Comput. Phys.* 227 (6) (2008) 3191–3211, <http://dx.doi.org/10.1016/j.jcp.2007.11.038>.
- [36] H.S. Udaykumar, W. Shyy, M.M. Rao, ELAFINT: a mixed Eulerian Lagrangian method for fluid flows with complex and moving boundaries, *Int. J. Numer. Methods Fluids* 22 (8) (1996) 691–712, [http://dx.doi.org/10.1002/\(SICI\)1097-0363\(19960430\)22:8<691::AID-FLD371>3.0.CO;2-U](http://dx.doi.org/10.1002/(SICI)1097-0363(19960430)22:8<691::AID-FLD371>3.0.CO;2-U).
- [37] C.S. Peskin, Numerical analysis of blood flow in the heart, *J. Comput. Phys.* 25 (3) (1977) 220–252, [http://dx.doi.org/10.1016/0021-9991\(77\)90100-0](http://dx.doi.org/10.1016/0021-9991(77)90100-0).
- [38] F. Gibou, R.P. Fedkiw, L.-T. Cheng, M. Kang, A second-order-accurate symmetric discretization of the Poisson equation on irregular domains, *J. Comput. Phys.* 176 (1) (2002) 205–227, <http://dx.doi.org/10.1006/jcph.2001.6977>.
- [39] Y. Sato, B. Ničeno, A sharp-interface phase change model for a mass-conservative interface tracking method, *J. Comput. Phys.* 249 (2013) 127–161, <http://dx.doi.org/10.1016/j.jcp.2013.04.035>.
- [40] G.R. Guedon, Two-Phase Heat and Mass Transfer Modeling: Flexible Numerical Methods for Energy Engineering Analyses, Ph.D. thesis, Politecnico Di Milano, Italy, 2013, <http://hdl.handle.net/10589/82788>.
- [41] W.M. Kays, M.E. Crawford, *Convective Heat and Mass Transfer*, third ed., McGraw–Hill, New York, USA, 1993.
- [42] P. Tsilingiris, Thermophysical and transport properties of humid air at temperature range between 0 and 100 °C, *Energy Convers. Manag.* 49 (5) (2008) 1098–1110, <http://dx.doi.org/10.1016/j.enconman.2007.09.015>.